



# Sulfur vacancy-rich MoS<sub>2</sub> as a catalyst for the hydrogenation of CO<sub>2</sub> to methanol

Jingting Hu<sup>1,2,7</sup>, Liang Yu<sup>2,3,7</sup>, Jiao Deng<sup>1,2,3</sup>, Yong Wang<sup>1,2</sup>, Kang Cheng<sup>1</sup>, Chao Ma<sup>4</sup>, Qinghong Zhang<sup>1</sup>, Wu Wen<sup>5</sup>, Shengsheng Yu<sup>5</sup>, Yang Pan<sup>5</sup>, Jiuzhong Yang<sup>5</sup>, Hao Ma<sup>6</sup>, Fei Qi<sup>6</sup>, Yongke Wang<sup>1</sup>, Yanping Zheng<sup>1</sup>, Mingshu Chen<sup>1</sup>, Rui Huang<sup>2</sup>, Shuhong Zhang<sup>1</sup>, Zhenchao Zhao<sup>2,3</sup>, Jun Mao<sup>1,2</sup>, Xiangyu Meng<sup>2,3</sup>, Qinqin Ji<sup>2,3</sup>, Guangjin Hou<sup>2,3</sup>, Xiuwen Han<sup>2,3</sup>, Xinhe Bao<sup>2,3</sup>, Ye Wang<sup>1</sup>✉ and Dehui Deng<sup>1,2,3</sup>✉

**The low-temperature hydrogenation of CO<sub>2</sub> to methanol is of great significance for the recycling of this greenhouse gas to valuable products, however, it remains a great challenge due to the trade-off between catalytic activity and selectivity. Here, we report that CO<sub>2</sub> can dissociate at sulfur vacancies in MoS<sub>2</sub> nanosheets to yield surface-bound CO and O at room temperature, thus enabling a highly efficient low-temperature hydrogenation of CO<sub>2</sub> to methanol. Multiple in situ spectroscopic and microscopic characterizations combined with theoretical calculations demonstrated that in-plane sulfur vacancies drive the selective hydrogenation of CO<sub>2</sub> to methanol by inhibiting deep hydrogenolysis to methane, whereas edge vacancies facilitate excessive hydrogenation to methane. At 180 °C, the catalyst achieved a 94.3% methanol selectivity at a CO<sub>2</sub> conversion of 12.5% over the in-plane sulfur vacancy-rich MoS<sub>2</sub> nanosheets, which notably surpasses those of previously reported catalysts. This catalyst exhibited high stability for over 3,000 hours without any deactivation, rendering it a promising candidate for industrial application.**

The catalytic hydrogenation of CO<sub>2</sub> to methanol offers an attractive route for converting the greenhouse gas into value-added chemicals and mitigating the pressure on climate warming and the depletion of fossil fuels<sup>1–7</sup>. Establishing an energy-efficient catalytic process requires the development of high-performance catalysts capable of fulfilling a more energy-saving, low-temperature CO<sub>2</sub> hydrogenation process<sup>8,9</sup>. Metal oxide catalysts such as In<sub>2</sub>O<sub>3</sub> and ZnO/ZrO<sub>2</sub>, among others, typically require temperatures higher than 300 °C to catalyse the hydrogenation of CO<sub>2</sub> by a hydrogen-assisted dissociation mechanism<sup>10–12</sup>, leading to high energy consumption. Moreover, the reverse water-gas shift (RWGS) side reaction is difficult to avoid, leading to the formation of CO together with methanol<sup>13–16</sup>. Introducing transition metal components (for example, Cu, Pd and Ni) onto the metal oxides can enhance their activity at relatively low temperatures (<260 °C) by promoting the activation of H<sub>2</sub> (refs. 17–20), but at the same time this leads to a lower methanol selectivity owing to the excessive hydrogenation of CO<sub>2</sub> to methane and the RWGS reaction is exacerbated<sup>21–24</sup>. The barely controllable balance between C–O dissociation and H<sub>2</sub> activation severely restricts the simultaneous optimization of the catalytic activity and selectivity of the hydrogenation of CO<sub>2</sub> to methanol. Thus, it is a major challenge to develop an efficient catalyst for the highly selective hydrogenation of CO<sub>2</sub> to methanol at low temperature.

Here, we show that an in-plane sulfur vacancy-rich MoS<sub>2</sub> nanosheet catalyst can bypass such a restriction by on the one hand facilitating both CO<sub>2</sub> dissociation to surface-bound CO and O (CO\* and O\*) and H<sub>2</sub> activation on the sulfur vacancies, and on the other

hand promoting methanol formation over deep hydrogenolysis to methane, thereby enabling a highly efficient and selective hydrogenation of CO<sub>2</sub> to methanol at low temperature. At 180 °C, a methanol selectivity of 94.3% at a CO<sub>2</sub> conversion of 12.5% was achieved over the MoS<sub>2</sub> catalyst, which markedly surpasses those of previously reported catalysts, including the commercial Cu/ZnO/Al<sub>2</sub>O<sub>3</sub>. The catalyst showed high durability for over 3,000 hours in a stability test, without any decay in its activity and selectivity for methanol, thus exhibiting great potential for application in the large-scale synthesis of methanol from CO<sub>2</sub> hydrogenation.

## Results

**Performance of CO<sub>2</sub> conversion to methanol on MoS<sub>2</sub>.** CO<sub>2</sub> hydrogenation to methanol over a H<sub>2</sub>-pretreated few-layered MoS<sub>2</sub> nanosheet (FL-MoS<sub>2</sub>; Extended Data Fig. 1a–d) could be initiated even at room temperature, although the conversion was low (Fig. 1b), as supported by in situ diffuse reflectance infrared Fourier transform spectroscopy (DRIFTS) of the surface species showing the appearance of CO\*, O\* and CH<sub>3</sub>O\* peaks as the mixture of CO<sub>2</sub> and H<sub>2</sub> passed through the catalyst at 25 °C (Fig. 1a). In contrast, under an identical gaseous hourly space velocity (GHSV) over the commercial Cu/ZnO/Al<sub>2</sub>O<sub>3</sub> catalyst, as the benchmark for this reaction, a similar level of methanol production rate could be reached only at a temperature above 80 °C (Fig. 1b). As the temperature was increased, the FL-MoS<sub>2</sub> always delivered an extraordinary net methanol yield compared with Cu/ZnO/Al<sub>2</sub>O<sub>3</sub> and other state-of-the-art catalysts reported in the literature under

<sup>1</sup>State Key Laboratory of Physical Chemistry of Solid Surfaces, Collaborative Innovation Center of Chemistry for Energy Materials, College of Chemistry and Chemical Engineering, Xiamen University, Xiamen, China. <sup>2</sup>State Key Laboratory of Catalysis, Collaborative Innovation Center of Chemistry for Energy Materials, Dalian Institute of Chemical Physics, Chinese Academy of Sciences, Dalian, China. <sup>3</sup>University of Chinese Academy of Sciences, Beijing, China.

<sup>4</sup>Center for High-Resolution Electron Microscopy, College of Materials Science and Engineering, Hunan University, Changsha, China. <sup>5</sup>National Synchrotron Radiation Laboratory, University of Science and Technology of China, Hefei, China. <sup>6</sup>Key Laboratory for Power Machinery and Engineering of MOE, Shanghai Jiao Tong University, Shanghai, China. <sup>7</sup>These authors contributed equally: Jingting Hu, Liang Yu. ✉e-mail: [wangye@xmu.edu.cn](mailto:wangye@xmu.edu.cn); [dhdeng@dicp.ac.cn](mailto:dhdeng@dicp.ac.cn)

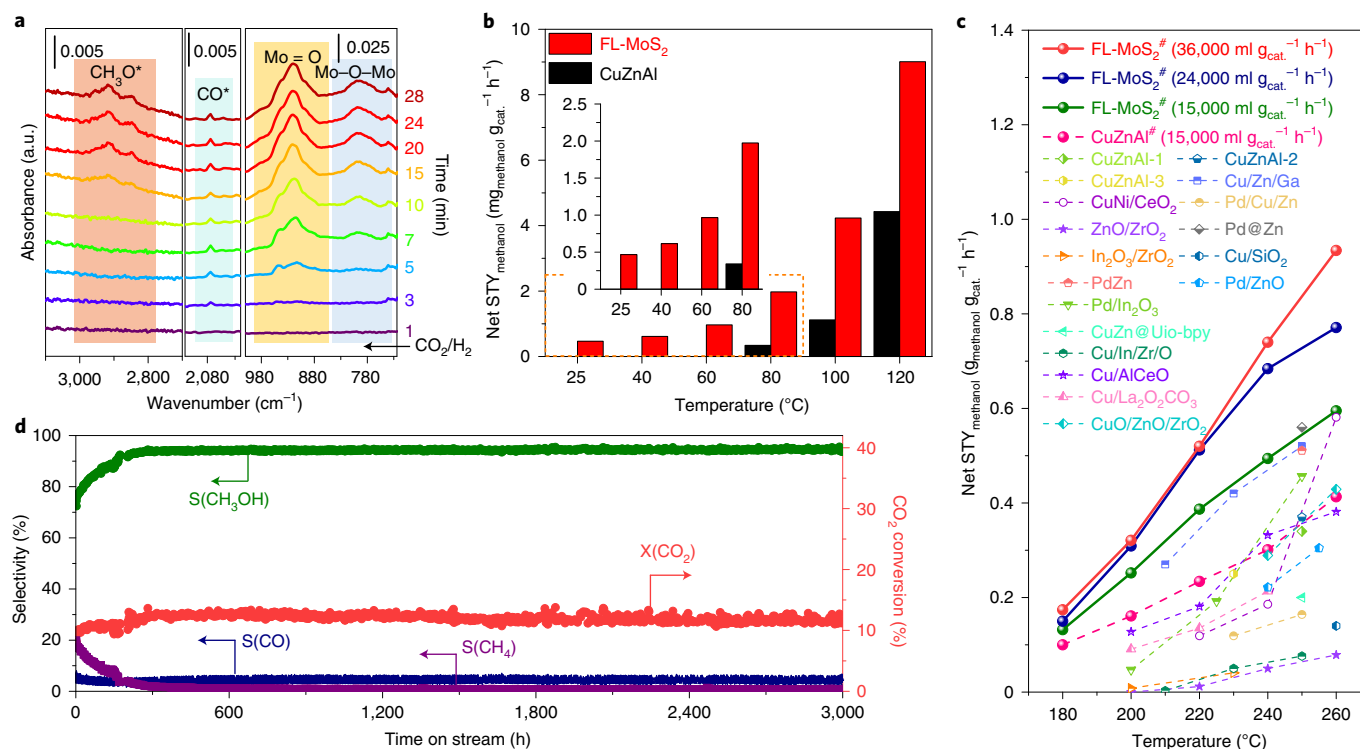


**Fig. 1 | Catalytic properties of different catalysts in CO<sub>2</sub> hydrogenation to methanol. a**, In situ DRIFT spectra of CO<sub>2</sub> hydrogenation over the FL-MoS<sub>2</sub> catalyst at room temperature (25 °C). Mo=O and Mo–O–Mo are O\* species. The arrowed CO<sub>2</sub>/H<sub>2</sub> denotes the introduction of the gas mixture into the reactor. The vertical black line segments are scale bars for the absorbance. **b**, Comparison of net space-time-yield of methanol (STY<sub>methanol</sub>, calculated based on the amount of catalyst) on the Cu/ZnO/Al<sub>2</sub>O<sub>3</sub> (CuZnAl) and FL-MoS<sub>2</sub> catalysts from 25 to 120 °C at a GHSV of 1,500 ml g<sub>cat</sub><sup>-1</sup> h<sup>-1</sup>. The inset shows an enlargement of the dashed box area. **c**, Comparison of the net STY<sub>methanol</sub> over the FL-MoS<sub>2</sub> and other state-of-the-art catalysts under similar reaction conditions (see Supplementary Table 1 for more details; # indicates data from this work). **d**, Stability test of the FL-MoS<sub>2</sub> catalyst in the CO<sub>2</sub> hydrogenation reaction at 3,000 ml g<sub>cat</sub><sup>-1</sup> h<sup>-1</sup>, measuring the selectivity (S) and conversion (X) over 3,000 h. The conversion was far below the equilibrium conversion of around 40% at 180 °C (Extended Data Fig. 1l). The catalysts were pretreated in situ with H<sub>2</sub> at 300 °C for 3 h. The activity tests were performed using a tubular fixed-bed reactor at 50 bar and a H<sub>2</sub>/CO<sub>2</sub> ratio of 3:1.

similar reaction conditions (Fig. 1c, Extended Data Fig. 2a and Supplementary Table 1, calculations were based on the amount of catalyst). The intrinsic catalytic activity of the FL-MoS<sub>2</sub> catalyst was evaluated using the forward turnover frequency (TOF<sub>fwd</sub>) for methanol formation, and compared with the average TOF<sub>fwd</sub> over the Cu/ZnO/Al<sub>2</sub>O<sub>3</sub> catalyst at isoconversion levels (Extended Data Fig. 2b, TOF calculations were based on the amount of exposed metal atoms or S vacancies). Although the high activity of a small fraction of surface synergetic sites may not be captured for the Cu/ZnO/Al<sub>2</sub>O<sub>3</sub> catalyst in such a comparison<sup>25–31</sup>, the high TOF<sub>fwd</sub> over FL-MoS<sub>2</sub> still reveals the excellent activity of the catalyst. Moreover, the FL-MoS<sub>2</sub> catalyst also exhibits a remarkably high net TOF compared with the reported values for fixed-bed CO<sub>2</sub> hydrogenation (TOF was calculated based on the amount of exposed metal atoms or S vacancies; Extended Data Fig. 2c and Supplementary Table 2).

The FL-MoS<sub>2</sub> catalyst showed a high selectivity for CO<sub>2</sub> hydrogenation to methanol. At 180 °C, a methanol selectivity of 94.3% was achieved at a CO<sub>2</sub> conversion of 12.5% over the FL-MoS<sub>2</sub> catalyst, which is considerably higher than the value of 80.9% at 4.2% CO<sub>2</sub> conversion over the Cu/ZnO/Al<sub>2</sub>O<sub>3</sub> catalyst under identical reaction conditions (Extended Data Fig. 2d), and significantly surpasses those of previously reported catalysts. In addition, at different CO<sub>2</sub> conversion levels, the methanol selectivity over the FL-MoS<sub>2</sub> catalyst was always higher than that over the Cu/ZnO/Al<sub>2</sub>O<sub>3</sub> catalyst at the same temperature (Extended Data Fig. 2e). The activity of the FL-MoS<sub>2</sub> catalyst was well reproduced using seven batches of

individually synthesized FL-MoS<sub>2</sub> catalyst. The fluctuations in both CO<sub>2</sub> conversion and methanol selectivity were less than 3% (Extended Data Fig. 1m).

The long-term stability test of the FL-MoS<sub>2</sub> catalyst showed no signs of decay in either the activity or methanol selectivity over 3,000 hours at 180 °C, with a stable conversion of around 12.5% (Fig. 1d). In addition, the stability was well maintained for more than 600 hours even at 260 °C (Extended Data Fig. 1n). Statistical analysis of the layer number of the fresh and used FL-MoS<sub>2</sub> catalyst, based on high-resolution transmission electron microscopy (HRTEM), showed a slight increase in the layer thickness after 3,000 hours of the durability test, which indicates a small degree of aggregation of the MoS<sub>2</sub> layers (Extended Data Fig. 1e–j). This may be caused by an increase in the surface energy of the basal plane due to the generation of in-plane sulfur vacancies during the hydrogenation reaction. Nevertheless, no visible difference in the crystallographic structure of the FL-MoS<sub>2</sub> catalyst was observed by powder X-ray diffraction (XRD) analysis after 3,000 hours of the durability test compared with that of the fresh catalyst (Extended Data Fig. 1k). This indicates that the FL-MoS<sub>2</sub> is a robust catalyst for the low-temperature hydrogenation of CO<sub>2</sub> to methanol, exhibiting great potential for application as an energy-saving industrial process.

**Identifying the active sites of MoS<sub>2</sub>.** H<sub>2</sub> pretreatment increased substantially the catalytic performance of FL-MoS<sub>2</sub>, with the forward reaction rate ( $r_f$ ) for methanol formation (0.132 g<sub>methanol</sub> g<sub>cat</sub><sup>-1</sup> h<sup>-1</sup>)

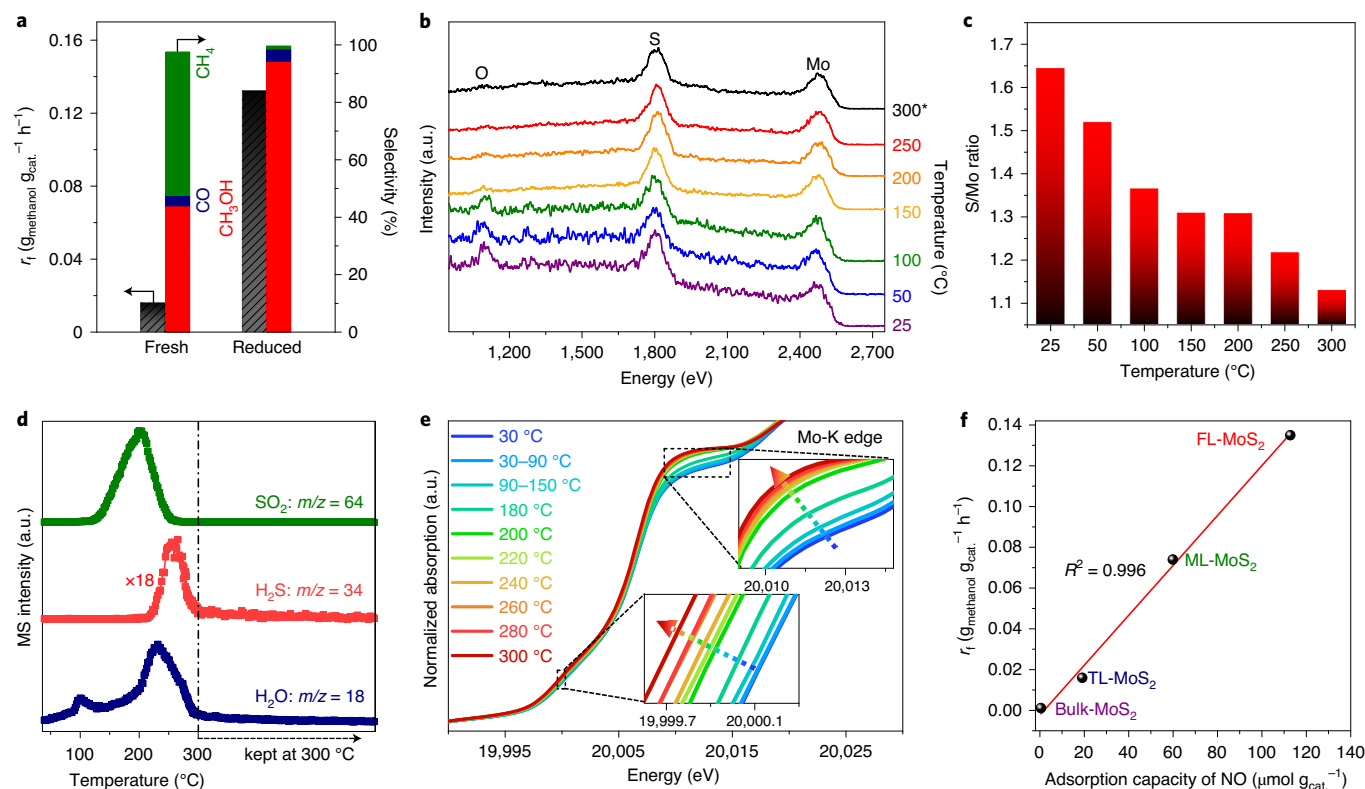


**Fig. 2 | Identification of the active sites of the MoS<sub>2</sub> catalyst for CO<sub>2</sub> hydrogenation to methanol.** **a**, Contrastive catalytic performances, showing the forward reaction rate and selectivity, of the FL-MoS<sub>2</sub> catalyst before (fresh) and after (reduced) H<sub>2</sub> pretreatment at 300 °C for 3 h. For the fresh FL-MoS<sub>2</sub> catalyst, the data obtained after about 4 h of reaction were used in the discussion. Reaction activity tests were performed using a tubular fixed-bed reactor at 50 bar, 180 °C and a H<sub>2</sub>/CO<sub>2</sub> ratio of 3:1. **b**, HS-LEIS (He<sup>+</sup>) spectra of the FL-MoS<sub>2</sub> catalyst after H<sub>2</sub> reduction at different temperatures, which have been normalized to the Mo peak. **c**, S/Mo HS-LEIS peak area ratios for the FL-MoS<sub>2</sub> catalyst after reduction at different temperatures. Before testing, samples were reduced for 1 h at temperatures from 50 to 250 °C and for 3 h at 300 °C. **d**, In situ SVUV-PIMS detection of the H<sub>2</sub> pretreatment products. **e**, Variation of the in situ Mo K-edge XANES spectra of the FL-MoS<sub>2</sub> catalyst following H<sub>2</sub> pretreatment at different temperatures. **f**, Correlation between the forward reaction rate ( $r_f$ ) for methanol formation and the density of S vacancies of different MoS<sub>2</sub> catalysts. The density of S vacancies is measured as the specific adsorption capacity of NO.

at 2.5% CO<sub>2</sub> conversion over the H<sub>2</sub>-pretreated FL-MoS<sub>2</sub> catalyst being almost ten times that over the fresh catalyst (0.016 g<sub>methanol</sub> g<sub>cat.</sub><sup>-1</sup> h<sup>-1</sup>) at 3.1% CO<sub>2</sub> conversion (Fig. 2a). High-sensitivity low-energy ion scattering spectroscopy (HS-LEIS) showed the disappearance of the O peak and a decrease in the S/Mo peak area ratio from 1.64 to 1.13 as the temperature of the quasi in situ H<sub>2</sub> treatment of the FL-MoS<sub>2</sub> catalyst increased (Fig. 2b,c). Signals of SO<sub>2</sub>, H<sub>2</sub>O and H<sub>2</sub>S were directly detected in the reduction process by in situ synchrotron-based VUV photoionization mass spectrometry (SVUV-PIMS; Fig. 2d), which indicates the removal of O atoms and some S atoms from MoS<sub>2</sub> by the H<sub>2</sub> pretreatment. The O atoms may come from oxidation of the MoS<sub>2</sub> during the synthetic process or when the material is exposed to the air. X-ray photoelectron spectroscopy (XPS) of the as-synthesized FL-MoS<sub>2</sub> catalyst showed only two S 2*p* peaks, attributed to intact lattice S and oxidized lattice S in MoS<sub>2</sub> (Extended Data Fig. 3d), and no excess stoichiometric S was observed. Therefore, the removal of S by H<sub>2</sub> reduction leads to the formation of S vacancies and the exposure of coordinatively unsaturated Mo atoms. This was further confirmed by in situ X-ray absorption near-edge structure (XANES) characterization showing that the absorption edge of the Mo K edge shifts to a lower energy level owing to the reduction of FL-MoS<sub>2</sub> (Fig. 2e). Furthermore, in situ electron paramagnetic resonance (EPR) spectra<sup>32,33</sup> displayed an obvious increase in the density of S vacancies after H<sub>2</sub> reduction of the FL-MoS<sub>2</sub> (Extended Data Fig. 3a). These results indi-

cate that the S vacancies are a key factor in the catalytic activity for CO<sub>2</sub> hydrogenation to methanol. The reaction itself generated more S vacancies over the MoS<sub>2</sub> catalyst, as reflected by the in situ EPR and XPS characterization of the FL-MoS<sub>2</sub> catalyst before and after the reaction, with the used catalyst exhibiting increased EPR signal intensity and a decreased S/Mo atomic ratio compared with the H<sub>2</sub>-reduced fresh catalyst (Extended Data Fig. 3a,e). This could be the reason for the existence of an induction period in the initial stage of the reaction process, which shows a gradual improvement in the catalytic activity (Fig. 1d).

To further confirm the role of S vacancies as the active sites for the catalytic process, MoS<sub>2</sub> nanosheet catalysts with different concentrations of S vacancies were designed to investigate the relationship between the density of sulfur vacancies and the reaction rate. Beside FL-MoS<sub>2</sub>, multilayered MoS<sub>2</sub> (ML-MoS<sub>2</sub>) and thick-layered MoS<sub>2</sub> (TL-MoS<sub>2</sub>) were synthesized using a layer-controlling method, and commercial MoS<sub>2</sub> was adopted as reference, representing bulk MoS<sub>2</sub> (Bulk-MoS<sub>2</sub>; Extended Data Fig. 4a–i). All these MoS<sub>2</sub> catalysts present large lateral sizes and exhibited similar methanol selectivity (>80%) in the CO<sub>2</sub> hydrogenation reaction (Extended Data Fig. 4p). The density of S vacancies in these samples after H<sub>2</sub> pretreatment were quantified in terms of the density of single electrons by in situ EPR spectroscopy and the specific adsorption capacity of NO by in situ NO pulse adsorption<sup>34,35</sup>. Experiments exploring the catalytic performances of these catalysts revealed that

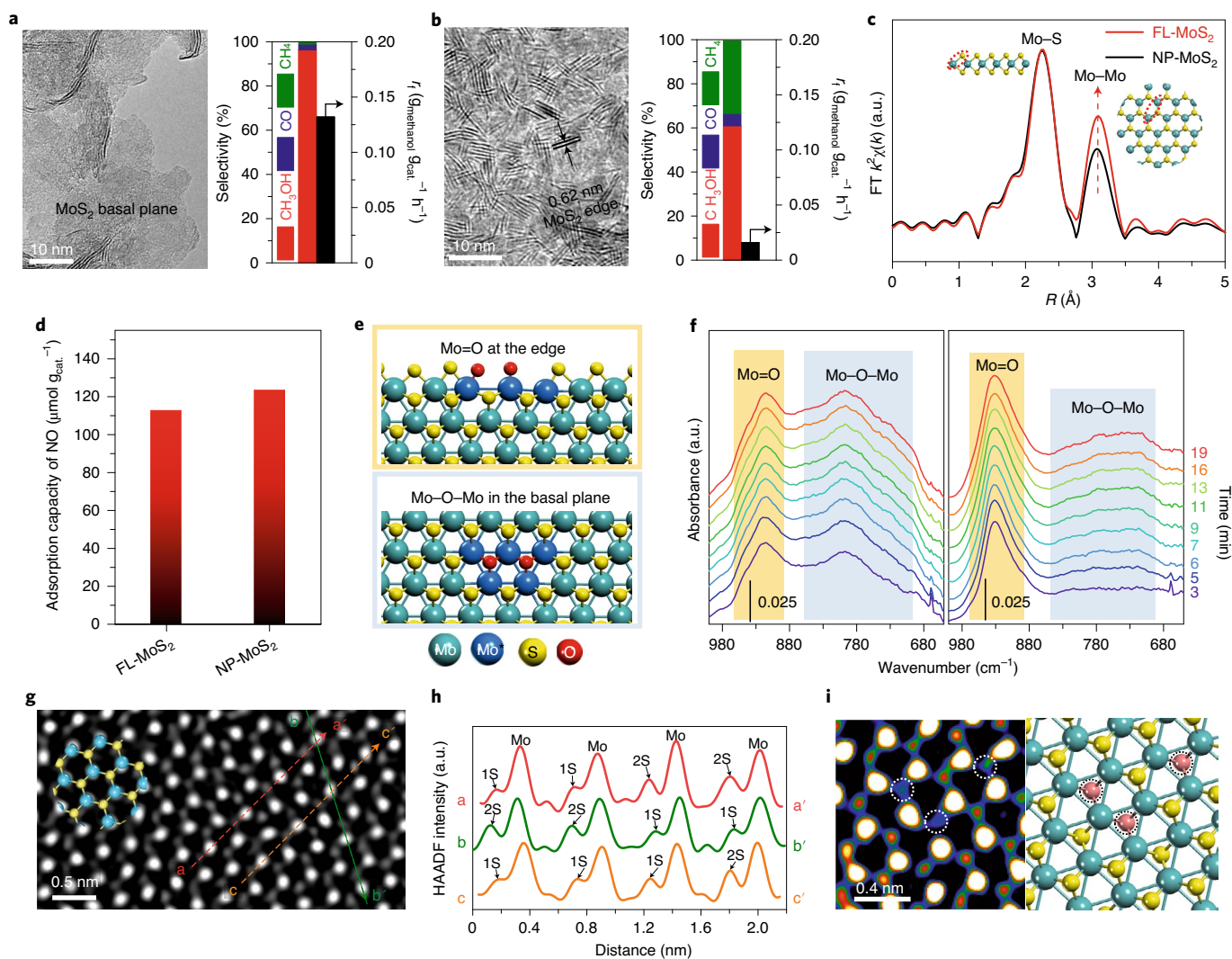


**Fig. 3 | Role of in-plane and edge S vacancies in catalysing CO<sub>2</sub> hydrogenation to methanol.** **a, b**, HRTEM images (left) and the corresponding catalytic performances (right) of the basal plane-dominant FL-MoS<sub>2</sub> catalyst (**a**) and edge-dominant NP-MoS<sub>2</sub> catalyst (**b**) at an isoconversion of 2.4–2.5%. The catalysts were pretreated in situ with H<sub>2</sub> at 300 °C for 3 h. Reaction activity tests were performed using a tubular fixed-bed reactor at 50 bar, 180 °C and a H<sub>2</sub>/CO<sub>2</sub> ratio of 3:1. The GHSV values were 15,000 and 3,000 ml<sub>g<sub>cat.</sub></sub><sup>-1</sup> h<sup>-1</sup> for the FL-MoS<sub>2</sub> and NP-MoS<sub>2</sub> catalysts, respectively. **c**, Fourier-transformed (FT) EXAFS spectra of the FL-MoS<sub>2</sub> and NP-MoS<sub>2</sub> catalysts. The insets show the atomic structures of the FL-MoS<sub>2</sub> and NP-MoS<sub>2</sub> catalysts with dotted lines denoting the Mo-S shell (left) and Mo-Mo shell (right). **d**, Adsorption capacity of NO on the reduced FL-MoS<sub>2</sub> and NP-MoS<sub>2</sub> catalysts. **e**, DFT-calculated structures of the adsorption of oxygen at the edge (top) and in-plane (bottom) S vacancies. **f**, In situ DRIFTS spectra of the FL-MoS<sub>2</sub> (left) and NP-MoS<sub>2</sub> (right) catalysts during the O<sub>2</sub> adsorption process. The vertical black line segments are scale bars for the absorbance. **g**, HAADF-STEM image of the basal plane of the FL-MoS<sub>2</sub> catalyst after the reaction. **h**, HAADF intensity profiles along the corresponding dashed lines in **g**. The labels 1S and 2S denote one sulfur and two sulfur atoms, respectively. **i**, HAADF-STEM image (left) and the corresponding atomic structure (right) of the FL-MoS<sub>2</sub> catalyst showing the S vacancies (in dotted lines and pink balls).

the  $r_f$  value for methanol formation is closely related to the density of S vacancies in MoS<sub>2</sub>, with a higher density of S vacancies leading to a higher production rate of methanol (Fig. 2f and Extended Data Fig. 4j,k). No linear relation was found between  $r_f$  and the Brunauer–Emmett–Teller surface area of these samples (Extended Data Fig. 4l,m). These results demonstrate that the activity of MoS<sub>2</sub> for CO<sub>2</sub> hydrogenation to methanol is derived from the S vacancies.

H<sub>2</sub> pretreatment could remove S atoms both from the basal plane and edges of the MoS<sub>2</sub> lattice and thereby lead to the coexistence of in-plane and edge S vacancies. To clarify the effect of in-plane and edge S vacancies in catalysing CO<sub>2</sub> hydrogenation to methanol, we synthesized a nanoporous MoS<sub>2</sub> catalyst (NP-MoS<sub>2</sub>) in which the MoS<sub>2</sub> nanosheets have small lateral sizes with abundant edges,

as shown in the HRTEM images as well as in the extended X-ray absorption fine structure (EXAFS) spectra, indicating reduced Mo–Mo coordination (Fig. 3a–c and Extended Data Fig. 5a–e). The density of S vacancies in the NP-MoS<sub>2</sub> catalyst was then quantified in situ through the specific adsorption capacity of NO<sup>34,35</sup>, with a value of 123.5 μmol<sub>g<sub>cat.</sub></sub><sup>-1</sup>, comparable to that of 112.8 μmol<sub>g<sub>cat.</sub></sub><sup>-1</sup> for the FL-MoS<sub>2</sub> catalyst (Fig. 3d). O<sub>2</sub> adsorption was employed to probe the dominating type of S vacancies in the two samples. With similar specific adsorption capacities of O<sub>2</sub> (Extended Data Fig. 5f), the in situ DRIFTS spectra of the NP-MoS<sub>2</sub> and FL-MoS<sub>2</sub> catalysts after O<sub>2</sub> adsorption revealed the two samples to have markedly different oxygen adsorption features (Fig. 3f). The absorption peaks at 900–960 cm<sup>-1</sup> and broad band at 700–860 cm<sup>-1</sup> have been assigned

to the vibrations of Mo=O and Mo–O–Mo species<sup>36</sup>, respectively. Density functional theory (DFT) calculations showed that oxygen adsorbed at the edge and in-plane S vacancies are primarily in Mo=O and M–O–M configurations, respectively (Fig. 3e). These results indicate that the NP-MoS<sub>2</sub> catalyst enriched with Mo=O species mainly exposes edge S vacancies and that the FL-MoS<sub>2</sub> catalyst with apparently increased Mo–O–Mo species possesses more in-plane S vacancies. Comparing the catalytic performances of the FL-MoS<sub>2</sub> and NP-MoS<sub>2</sub> catalysts at isoconversion levels, the FL-MoS<sub>2</sub> catalyst always showed a higher methanol selectivity (Fig. 3a,b and Extended Data Fig. 5g,h), indicating that the in-plane S vacancies are more selective for the CO<sub>2</sub> hydrogenation to methanol.

To further confirm the role of the in-plane S vacancies in determining the methanol selectivity, the S vacancies of the in situ H<sub>2</sub>-reduced MoS<sub>2</sub> samples with different layer thicknesses were also quantitatively studied by <sup>31</sup>P magic-angle-spinning NMR (MAS NMR) spectroscopy using trimethylphosphine (TMP) as probe adsorbate<sup>37</sup>, which presented two resonance peaks near –9 and –22 ppm, implying two different adsorption sites (Extended Data Fig. 4n). DFT studies showed that TMP can be adsorbed only on S vacancies. The <sup>31</sup>P chemical shifts of TMP adsorbed on both in-plane and edge S vacancies were calculated by DFT methods after the structures were fully optimized; the TMP molecules adsorbed on the Mo-edge S vacancies were found to possess a higher chemical shift tensor on average than those of TMP at the in-plane S vacancies (Extended Data Fig. 6a,b). We further analysed the number of electrons on the P atoms of the TMP adsorbed on the in-plane and Mo-edge S vacancies, which were on average 1.60 and 1.70 e<sup>–</sup>, respectively. A higher electron density can lead to a greater shielding tensor for the nuclei, and hence a higher resonance magnetic field. Therefore, the downfield (–9 ppm) and upfield (–22 ppm) peaks can be assigned to the in-plane and edge S vacancies, respectively. Thus, the density of in-plane and edge S vacancies can be relatively quantified in units of the specific adsorption capacity of TMP (Extended Data Fig. 4p). The explicit linear correlation between the density of in-plane vacancies and *r<sub>f</sub>* for methanol formation demonstrates that the in-plane S vacancies favour CO<sub>2</sub> hydrogenation to methanol more than the edge S vacancies (Extended Data Fig. 4o).

The existence of in-plane S vacancies in the FL-MoS<sub>2</sub> catalyst was confirmed using high-angle annular dark-field scanning transmission electron microscopy (HAADF-STEM)<sup>32,38</sup>. Figure 3g presents a wide-field HAADF-STEM view of the FL-MoS<sub>2</sub> basal plane, exhibiting a characteristic hexagonal pattern of 2H-MoS<sub>2</sub>. Intensity profile analysis of the HAADF-STEM image along imaginary line demonstrates the existence of S vacancies (Fig. 3g,h). A typical distribution of S vacancies is illustrated in Fig. 3i, showing a cluster of S vacancies in the basal plane of the FL-MoS<sub>2</sub> catalyst.

**Reaction mechanisms of CO<sub>2</sub> hydrogenation.** To understand the structure-dependent activity of MoS<sub>2</sub> in the hydrogenation of CO<sub>2</sub> to methanol at an atomic level, DFT calculations were performed to study the underlying reaction mechanisms at the in-plane and edge S vacancies. A periodic trilayer model of MoS<sub>2</sub> and a nanoribbon model of MoS<sub>2</sub>, with the Mo edge saturated with S monomers and the S edge saturated with a combination of S monomers and dimers, were adopted as the initial structures for generating the in-plane and edge S vacancies, respectively (Extended Data Fig. 7a,b)<sup>39,40</sup>. Models of single S vacancy (single-Sv), double S vacancy (double-Sv) and triple S vacancy (triple-Sv) were employed to simulate the reaction process for both the in-plane and edge cases (Extended Data Fig. 7c).

The single-Sv at the edge or in the basal plane can barely adsorb CO<sub>2</sub>. However, CO<sub>2</sub> can be adsorbed on the double-Sv and triple-Sv sites, either in the basal plane or at the Mo edge, and readily dissociates to CO\* and O\* with low barriers of below 0.33 eV (Fig. 4a,b and Extended Data Fig. 8a,b). In comparison, the hydrogenation of

CO<sub>2</sub> to COOH\* or HCOO\* at the in-plane S vacancy (Sv) sites is less favourable with clearly higher barriers, which contrasts with the dominant mechanisms on metal oxide or metal/metal oxide catalysts<sup>8,10,12,22,41,42</sup>. This is consistent with the observation of CO\* and O\* signals in the in situ DRIFTS spectrum at room temperature (Extended Data Fig. 9a,b) and a slight increase in the Mo oxidation state in the in situ XANES spectrum at 180 °C (Extended Data Fig. 9h) when pure CO<sub>2</sub> was introduced into the H<sub>2</sub>-pretreated FL-MoS<sub>2</sub> and NP-MoS<sub>2</sub> catalysts. At the Mo-edge double-Sv site, the formation of HCOO\* is competitive with the CO<sub>2</sub> dissociation step, but further hydrogenation or dissociation of HCOO\* is relatively difficult, with energy barriers of over 1.1 eV, and thus are likely to be depressed. In the steps following CO<sub>2</sub> dissociation, CO\* desorption from either the in-plane or Mo-edge Sv sites requires higher activation energies than CO\* hydrogenation to CHO\*. Further hydrogenation of CHO\* to CH<sub>3</sub>OH via CH<sub>2</sub>O\* and CH<sub>3</sub>O\* intermediates all have remarkably lower energy barriers than the corresponding C–O bond-breaking steps at both the in-plane and Mo-edge Sv sites (Fig. 4a,b and Extended Data Fig. 8a,b). Such reaction paths agree well with the high-pressure in situ DRIFTS characterization of the hydrogenation process. When the feeding gas was switched from pure CO<sub>2</sub> to H<sub>2</sub> at 180 °C and 30 bar, the CO\* peaks from the dissociation of CO<sub>2</sub> (Extended Data Fig. 9f) gradually disappeared with the rise of CH<sub>3</sub>O\* peaks, the intensity of which first increased and then decreased as time went on (Extended Data Fig. 9g), thereby indicating the hydrogenation of CO\* to CH<sub>3</sub>O\* and then the formation of CH<sub>3</sub>OH. The in situ SVUV-PIMS (Extended Data Fig. 9i,j) and in situ DRIFTS analyses of the reaction process (Extended Data Fig. 9c–e) showed signals of desorbed HCHO and CH<sub>3</sub>O\* surface species, respectively, also supporting the proposed reaction mechanism.

However, the Mo-edge and in-plane Sv sites exhibit different reactivities for the dissociation of the generated CH<sub>3</sub>OH\*. The desorption of CH<sub>3</sub>OH\* from the Mo-edge double-Sv and triple-Sv sites is less favourable, being endergonic in free energy by around 0.6 eV, compared with desorption from the in-plane Sv sites, being exergonic by more than 0.5 eV (Fig. 4a,b and Extended Data Fig. 8a,b). By contrast, the dissociation of CH<sub>3</sub>OH\* to CH<sub>3</sub>\* and OH\* at the Mo-edge double-Sv and triple-Sv sites is more favourable, with notably lower barriers of around 1.1 eV compared with values of around 1.8 eV at the in-plane Sv sites (Fig. 4a,b and Extended Data Fig. 8a,b). The Sv at the corner (Corner-Sv) of the Mo edge also show good activity for the dissociation of methanol, with a barrier of 1.04 eV. These results indicate that the production of CH<sub>3</sub>OH is energetically more favourable at the in-plane Sv sites than at the Mo-edge Sv sites, where CH<sub>4</sub> formation is more competitive.

On the basis of the above reaction mechanisms, reaction microkinetic modelling of the CO<sub>2</sub> hydrogenation process at the in-plane and Mo-edge Sv sites was conducted using CatMAP<sup>43</sup>. The results show that at the in-plane Sv sites, CH<sub>3</sub>OH formation is more favourable with higher turnover frequencies (TOFs) than the formation of CO and CH<sub>4</sub> over a wide range of temperatures and pressures. However, CH<sub>4</sub> formation is facilitated at the Mo-edge Sv sites with even higher TOFs than those for CH<sub>3</sub>OH formation (Fig. 4c,d and Extended Data Fig. 8c,d). These results agree well with the experimental observations that the FL-MoS<sub>2</sub> catalyst is more selective toward CH<sub>3</sub>OH formation whereas the NP-MoS<sub>2</sub> catalyst is more selective for CH<sub>4</sub> formation.

To verify the theoretical finding that the Mo-edge Sv sites are more reactive toward CH<sub>3</sub>OH dissociation than the in-plane Sv sites, CH<sub>3</sub>OH decomposition in H<sub>2</sub> was investigated experimentally (Extended Data Fig. 5i); the results showed that the conversion rate of CH<sub>3</sub>OH to CH<sub>4</sub> over the NP-MoS<sub>2</sub> catalyst is clearly higher than that over the FL-MoS<sub>2</sub> catalyst. This is in good agreement with the theoretical modelling of the CH<sub>3</sub>OH reduction reaction microkinetics, which showed higher TOFs for CH<sub>4</sub> formation on the Mo-edge

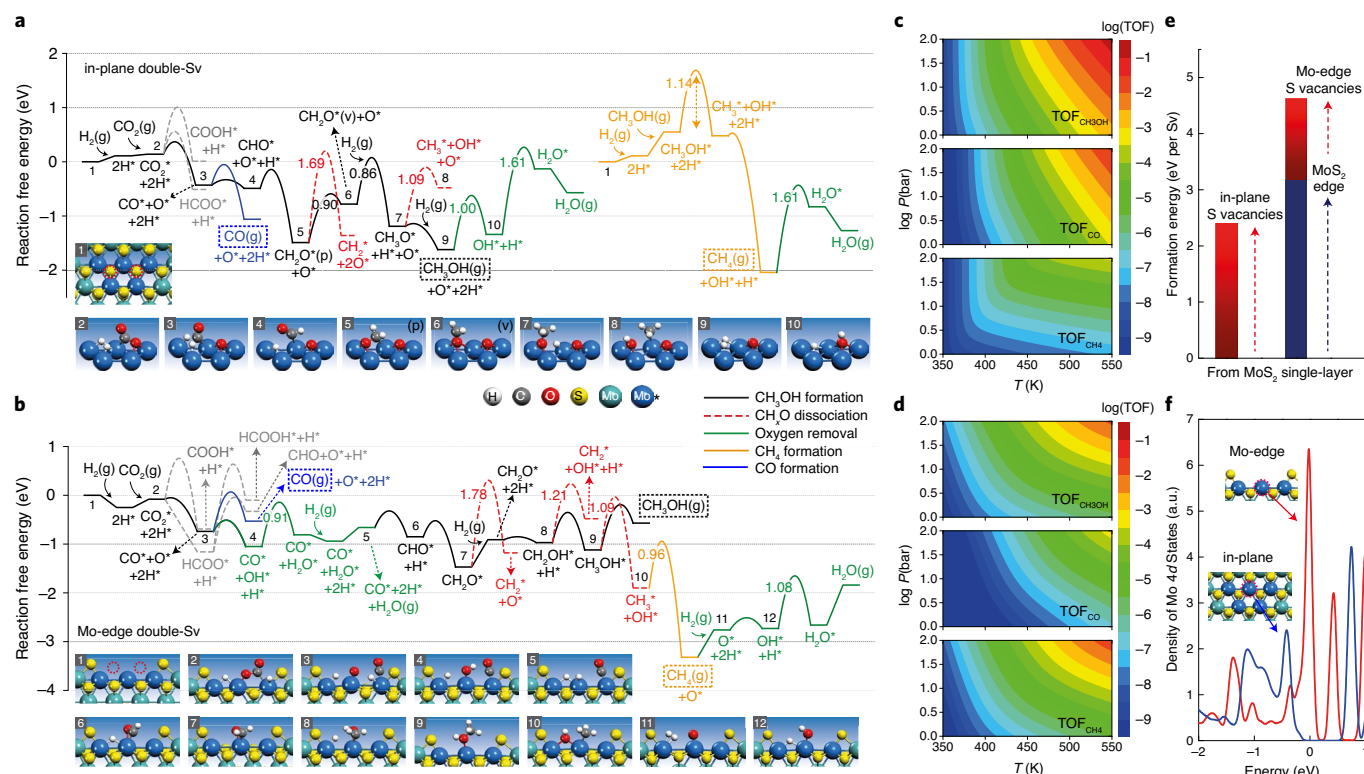


**Fig. 4 | DFT studies of the reaction mechanisms of CO<sub>2</sub> hydrogenation on the double-Sv of MoS<sub>2</sub>.** **a, b**, Free-energy diagrams of the CO<sub>2</sub> hydrogenation reaction pathways on the in-plane (**a**) and Mo-edge (**b**) double-Sv. The insets show the atomic structures of the Sv and the reaction intermediates. The red dotted circles in structure 1 denote the positions of the Sv. The labels (g), (p) and (v) represent gas phase, parallelly adsorbed, and vertically adsorbed states, respectively. **c, d**, TOFs for the generation of CH<sub>3</sub>OH, CO and CH<sub>4</sub> from the microkinetic modelling of the reaction mechanisms at the in-plane (**c**) and Mo-edge (**d**) double-Sv. **e**, Comparison of the formation energies of an in-plane Sv and Mo-edge Sv relative to the two-dimensional periodic MoS<sub>2</sub> single layer as reference. **f**, Electronic density of states of the Mo 4d orbitals at the in-plane and Mo-edge double-Sv. The Fermi level is located at 0 eV.

Sv sites than on the in-plane Sv sites (Extended Data Fig. 10). The higher reactivity of the Mo-edge Sv sites toward methanol decomposition is probably due to the much higher formation energy compared with that of the in-plane Sv site (Fig. 4e). The coordinatively unsaturated Mo sites at the Mo-edge S vacancies possess a notably higher electron density of 4d states near the Fermi level, which leads to the overbinding of CH<sub>3</sub>OH\* and thereby a lower barrier for CH<sub>3</sub>OH\* dissociation, as discussed above (Fig. 4f).

## Conclusions

Edge sites of MoS<sub>2</sub> are widely reported to be the dominant active centres in many catalytic reactions<sup>40,44–47</sup>. In this study, however, the edge S vacancies led to undesired excessive hydrogenation of CO<sub>2</sub> to methane. By contrast, we have demonstrated the in-plane S vacancies of MoS<sub>2</sub> to be ideal active centres for a highly efficient, low-temperature CO<sub>2</sub> hydrogenation to methanol in preference to hydrogenolysis to methane. An excellent durability of over 3,000 hours characterizes the single component MoS<sub>2</sub> as a simple and promising catalyst for industrial applications. The findings in this work reveal the potential of in-plane vacancies of two-dimensional materials in catalysis, and could inspire the development of new catalysts for this reaction beyond metal or metal oxide catalysts, such as metal carbides, metal phosphides, metal nitrides and other metal sulfides<sup>48,49</sup>. This work also provides a prototype for obtaining targeted catalytic reactivity and selectivity by rationally tailoring the structure and atom vacancies.

## Methods

**Preparation of the FL-MoS<sub>2</sub> catalyst.** The FL-MoS<sub>2</sub> catalyst was synthesized by using our previously reported method<sup>50</sup>. Typically, 900 mg (NH<sub>4</sub>)<sub>6</sub>Mo<sub>7</sub>O<sub>24</sub>·4H<sub>2</sub>O was dissolved in 20 ml deionized water to form a homogeneous solution. Then, this solution and 10 ml CS<sub>2</sub> were sealed in a 40 ml stainless-steel autoclave under Ar protection and maintained at 400 °C for 4 h. The product was treated with 6 mol l<sup>-1</sup> KOH solution with stirring at 60 °C for 3 h, followed by washing with pure water and absolute ethanol several times and then drying at 80 °C.

**Evaluation of catalytic performance.** The catalytic reactions were performed in a high-pressure fixed-bed reactor built by Xiamen Han De Engineering. Typically, before the reaction, 200 mg catalyst with grain sizes of 250–600 μm was pretreated in situ with 30 ml min<sup>-1</sup> H<sub>2</sub> at 1 bar and 300 °C for 3 h. After the reduction, the reactant was introduced into the reactor. Argon was mixed into the H<sub>2</sub>/CO<sub>2</sub> mixture as an internal standard to calculate the CO<sub>2</sub> conversion. The reactions were performed under a pressure of 50 or 60 bar and in a temperature range from 25 to 280 °C, with a H<sub>2</sub>/CO<sub>2</sub> ratio of 3:1 and GHSVs from 1,500 to 54,000 ml g<sub>cat.</sub><sup>-1</sup> h<sup>-1</sup>.

The methanol decomposition experiments were performed in the same reactor with 200 mg catalyst. After the pre-reduction process as described above, liquid methanol (0.01 ml min<sup>-1</sup>) was fed into the reactor using a Series III Pump, meanwhile, high purity H<sub>2</sub> with 5% Ar was fed into the reactor at a gas flow rate of 30 ml min<sup>-1</sup> at 1 bar and 180 °C.

The products were analysed using an online gas chromatograph equipped with a thermal conductivity detector (TCD) and a flame ionization detector (FID). A TDX-01 packed column was connected to the TCD and an RT-Q-BOND-PL0T capillary column was connected to the FID. Product selectivity was calculated on a molar carbon basis. The catalytic performances during the stable phase of the reaction were typically used for discussion. For the fresh FL-MoS<sub>2</sub> catalyst without H<sub>2</sub> pretreatment, the data obtained after about 4 h of reaction were used for discussion.

The forward reaction rate ( $r_f$ ) was calculated on the basis of the measured net reaction rate ( $r_n$ ) and equilibrium factor ( $\eta$ )<sup>51</sup>:

$$r_f = r_n / (1 - \eta) \quad (1)$$

For the reaction  $\text{CO}_2(\text{g}) + 3\text{H}_2(\text{g}) \rightleftharpoons \text{CH}_3\text{OH}(\text{g}) + \text{H}_2\text{O}(\text{g})$ ,  $\eta$  was calculated using

$$\eta = \frac{P_{\text{CH}_3\text{OH}} \times P_{\text{H}_2\text{O}}}{P_{\text{CO}_2} \times P_{\text{H}_2}^3} \times \frac{1}{K} \quad (2)$$

where  $P_x$  is the partial pressure of species  $x$  (in atm) and  $K$  is the equilibrium constant for the reaction, which is  $1.806 \times 10^{-1} \text{ atm}^{-2}$  at  $180^\circ\text{C}$ ,  $9.598 \times 10^{-5} \text{ atm}^{-2}$  at  $200^\circ\text{C}$  and  $5.329 \times 10^{-5} \text{ atm}^{-2}$  at  $220^\circ\text{C}$ .

**Catalyst characterization.** Powder X-ray diffraction patterns were recorded on a Rigaku Ultima IV diffractometer with  $\text{Cu K}\alpha$  radiation ( $\lambda = 0.15406 \text{ nm}$ ) at  $40 \text{ kV}$  and  $30 \text{ mA}$ . The diffraction angles were scanned from  $5$  to  $85^\circ$  ( $2\theta$ ) at a speed of  $10^\circ \text{ min}^{-1}$ .

EPR spectroscopic measurements were performed on a Bruker A200 EPR spectrometer operated at X-band frequency with a microwave frequency of  $9.32 \text{ GHz}$ , a microwave power of  $10 \text{ mW}$  and a modulation frequency of  $100 \text{ kHz}$ . EPR characterization of the S vacancies was conducted using an in situ method, in which the samples were reduced and measured in the sample tube inside the EPR spectrometer, with no transfer of sample required during the whole process. Typically,  $30 \text{ mg}$  catalyst powder was placed in a quartz EPR sample tube. Before measurement, the catalyst, after  $\text{H}_2$  pretreatment for  $3 \text{ h}$  at  $300^\circ\text{C}$ , was purged with He at  $300^\circ\text{C}$  for  $2 \text{ h}$  to remove adsorbates. After running the catalytic reaction for  $4 \text{ h}$  at  $180^\circ\text{C}$ , the catalyst was first purged with  $\text{H}_2$  for  $2 \text{ h}$  and then heated to  $300^\circ\text{C}$  and purged with He for a further  $2 \text{ h}$ . All spectra were measured after cooling the samples to  $25^\circ\text{C}$  in a He atmosphere to allow comparison of the spectra. The gas flow rate during the EPR experiments was maintained at  $30 \text{ ml min}^{-1}$ . 1,1-Diphenyl-2-picrylhydrazyl was used as an external standard to estimate the density of sulfur vacancies in the  $\text{MoS}_2$  catalysts.

NO chemisorption measurements were performed on a Micromeritics Auto Chem II 2920 instrument. Typically,  $100 \text{ mg}$  sample was pretreated in situ with  $\text{H}_2$  at  $300^\circ\text{C}$  for  $3 \text{ h}$  and subsequently purged with He at  $300^\circ\text{C}$  for  $60 \text{ min}$ . NO chemisorption experiments were then performed at  $40^\circ\text{C}$  by pulsing  $0.5 \text{ ml}$  of  $2\%$   $\text{NO}/\text{He}$  ( $0.314 \mu\text{mol O}_2$  per pulse) through the catalyst every  $30 \text{ min}$ . The NO effluent (detected by mass spectrometer) increased to a constant value, signifying NO saturation of the catalyst, and then the total uptake of NO was calculated. The numbers of sulfur vacancies and exposed Mo atoms were calculated on the basis of the total uptake of NO, where one NO molecule corresponds to  $0.25 - 0.5$  sulfur vacancies or  $0.5 - 1.5$  exposed Mo atoms based on the results of DFT calculations (Extended Data Fig. 6c). Thus, the highest and lowest TOFs of the FL- $\text{MoS}_2$  catalyst were calculated on the basis of the amount of exposed sulfur vacancies or Mo atoms. Then, the average value of the highest and lowest TOFs was calculated as the TOF of the FL- $\text{MoS}_2$  catalyst.

$\text{O}_2$  chemisorption measurements were also performed on a Micromeritics Auto Chem II 2920 instrument. Typically,  $100 \text{ mg}$  sample was pretreated in situ with  $\text{H}_2$  at  $300^\circ\text{C}$  for  $3 \text{ h}$  and subsequently purged with He at  $300^\circ\text{C}$  for  $30 \text{ min}$ .  $\text{O}_2$  chemisorption experiments were then performed at  $40^\circ\text{C}$  by pulsing  $1 \text{ ml}$  of  $2.02\%$   $\text{O}_2/\text{Ar}$  ( $0.635 \mu\text{mol O}_2$  per pulse) over the catalyst every  $15 \text{ min}$ . The effluent  $\text{O}_2$  (detected by mass spectrometer) increased to a constant value, signifying  $\text{O}_2$  saturation of the catalyst, and the total uptake of  $\text{O}_2$  was then calculated.

$\text{N}_2\text{O}$  decomposition and  $\text{H}_2$  temperature-programmed reduction ( $\text{H}_2$ -TPR) were also performed on a Micromeritics Auto Chem II 2920 instrument equipped with a mass spectrometer and a TCD. Typically,  $100 \text{ mg}$   $\text{Cu}/\text{ZnO}/\text{Al}_2\text{O}_3$  was pretreated in situ with  $\text{H}_2$  at  $300^\circ\text{C}$  for  $3 \text{ h}$  and subsequently purged with He at  $300^\circ\text{C}$  for  $30 \text{ min}$ .  $\text{N}_2\text{O}$  decomposition was then performed at  $60^\circ\text{C}$  by pulsing  $1 \text{ ml N}_2\text{O}$  over the catalysts every  $15 \text{ min}$ . The effluent  $\text{N}_2\text{O}$  (detected by mass spectrometer) increased to a constant value, signifying that surface metallic Cu had been converted into  $\text{Cu}_2\text{O}$ . The reaction tube was then purged with He, and  $\text{H}_2$ -TPR was subsequently performed under a flow of  $5\%$   $\text{H}_2/\text{N}_2$  ( $30 \text{ ml min}^{-1}$ ) to  $300^\circ\text{C}$  at a ramp rate of  $10^\circ\text{C min}^{-1}$ .  $\text{H}_2$  consumption was measured by means of the TCD ( $\text{CuO}$  was used as external standard), and the amount of exposed metallic Cu was calculated on the basis of the  $\text{H}_2$  consumption<sup>52</sup>.

$^{31}\text{P}$  MAS NMR experiments were performed on a Bruker Ascend  $400 \text{ MHz}$  spectrometer at  $162 \text{ MHz}$  using a  $4\text{-mm}$  MAS NMR probe at a spinning rate of  $12 \text{ kHz}$ . The  $^{31}\text{P}$  MAS NMR spectra were accumulated over  $2,048$  scans with a  $\pi/4$  excitation pulse and a pulse delay of  $5 \text{ s}$ . The chemical shifts were referenced to  $85\%$   $\text{H}_3\text{PO}_4$ , and  $^{31}\text{P}$  NMR signals were calibrated against the signal of a known amount of  $(\text{NH}_4)_2\text{HPO}_4$ . For quantitative analysis,  $^{31}\text{P}$  MAS NMR spectra were acquired under the same conditions. Before measurement, samples were pretreated in situ with  $\text{H}_2$  at  $300^\circ\text{C}$  for  $3 \text{ h}$  and subsequently purged with He at  $300^\circ\text{C}$  for  $30 \text{ min}$ . Then, samples were transferred into a home-made adsorption device in a glove box and evacuated under high vacuum ( $10^{-4} \text{ Pa}$ ) for  $30 \text{ min}$  at room temperature ( $25^\circ\text{C}$ ). Thereafter, the samples were exposed to  $4 \text{ kPa}$  TMP, and the adsorption process performed for  $30 \text{ min}$ . Finally, the samples were evacuated at  $10^{-4} \text{ Pa}$  for  $30 \text{ min}$  to remove any excess and physically adsorbed TMP. The TMP-adsorbed samples were packed into the NMR rotor in a glove box to perform the NMR experiments.

HRTEM measurements were performed on a Phillips Analytical FEI Tecnai20 electron microscope operated at an accelerating voltage of  $200 \text{ kV}$ . The HAADF-STEM images were collected on a JEOL ARM-200F field-emission transmission electron microscope operated at an accelerating voltage of  $200 \text{ kV}$ .

The in situ SVUV-PIMS study was carried out on the mass spectrometry endstation of the National Synchrotron Radiation Laboratory at Hefei, China<sup>53,54</sup>. To detect the gas-phase products formed during the  $\text{H}_2$  pretreatment process,  $50 \text{ ml min}^{-1}$   $\text{H}_2$  was fed into the reactor, and the pressure inside the reactor was controlled at around  $32 \text{ torr}$ . Subsequently, the catalyst was heated to  $300^\circ\text{C}$  at a heating rate of  $5^\circ\text{C min}^{-1}$ , and the temperature was then held at  $300^\circ\text{C}$  for  $90 \text{ min}$ . The  $\text{H}_2$  pretreatment products were monitored at an ionization energy of  $12.8 \text{ eV}$ , which allowed the detection of  $\text{H}_2\text{S}$ ,  $\text{H}_2\text{O}$  and  $\text{SO}_2$ ; spectra were collected every  $30 \text{ s}$ . To detect the intermediates and products formed during  $\text{CO}_2$  hydrogenation, the reduced FL- $\text{MoS}_2$  catalyst was exposed to  $\text{H}_2/\text{CO}_2$  ( $3:1$ ) at a flow rate of  $80 \text{ ml min}^{-1}$  and a pressure of  $5 \text{ bar}$  at  $180^\circ\text{C}$ ; the photoionization efficiency spectra were collected for  $250 \text{ s}$  at ionization energies in the range  $10.6 - 11.6 \text{ eV}$  in steps of  $0.03 \text{ eV}$ .

X-ray absorption fine structure (XAFS) spectra were measured at the BL14W1 beamline of the Shanghai Synchrotron Radiation Facility. For the in situ XAFS experiments performed during the  $\text{H}_2$  pretreatment process, the first XAFS spectrum was collected at  $30^\circ\text{C}$ , then the reactor was heated to  $180^\circ\text{C}$ , and three spectra were collected during this process. After that, spectra were collected every  $20^\circ\text{C}$  until  $300^\circ\text{C}$ . For the in situ XAFS experiments performed during the  $\text{CO}_2$  hydrogenation process, after recording the spectrum of the fresh FL- $\text{MoS}_2$  catalyst, the catalyst was treated in situ with  $\text{H}_2$  at  $300^\circ\text{C}$  for  $3 \text{ h}$ . Then, the catalyst was cooled to  $180^\circ\text{C}$  under a  $\text{H}_2$  atmosphere, and the second spectrum was recorded. Next, the catalyst was exposed to  $30 \text{ ml min}^{-1}$   $\text{CO}_2$ , and the third spectrum was measured. Subsequently, the feeding gas was switched to  $30 \text{ ml min}^{-1}$   $\text{H}_2/\text{CO}_2$  ( $3:1$ ), and the fourth spectrum was recorded.

XPS measurements were carried out on an Omicron XPS System using Al  $\text{K}\alpha$  X-rays as the excitation source at a voltage of  $15 \text{ kV}$  and a power of  $300 \text{ W}$ .

HS-LEIS spectra were recorded using an Ion-TOF Qtac100 instrument<sup>55</sup>. To minimize the damage to the surface, helium was selected as the ion source with a kinetic energy of  $3 \text{ keV}$ , an ion flux of  $6,000 \text{ pA m}^{-2}$  and a spot size of  $2 \text{ mm} \times 2 \text{ mm}$ . After collecting the HS-LEIS spectrum of fresh FL- $\text{MoS}_2$ , the catalyst was transferred to the pretreatment chamber, pretreated with  $30 \text{ ml min}^{-1}$   $\text{H}_2$  at  $1 \text{ bar}$  and  $50, 100, 150, 200$  and  $250^\circ\text{C}$  for  $1 \text{ h}$  and at  $300^\circ\text{C}$  for  $3 \text{ h}$ , and then transferred to the analysis chamber for HS-LEIS measurement without exposing the samples to air. We used HS-LEIS to study the S/Mo ratios in the FL- $\text{MoS}_2$  samples before and after  $\text{H}_2$  reduction, rather than obtaining the absolute percentages of Mo and S atoms. Thus, calibration was not conducted.

In situ DRIFTS measurements were performed using a Fourier transform infrared (FTIR) spectrometer (Nicolet 6700 for atmospheric pressure tests and Vertex 70v for high-pressure tests) equipped with a mercury cadmium telluride detector. The in situ DRIFT spectra were recorded by collecting  $64$  scans at a resolution of  $4 \text{ cm}^{-1}$ . Before measurement, the catalysts were pretreated in situ with  $30 \text{ ml min}^{-1}$   $\text{H}_2$  at  $1 \text{ bar}$  and  $300^\circ\text{C}$  for  $3 \text{ h}$ . For the atmospheric pressure experiments, background spectra were recorded at  $25^\circ\text{C}$  in a flow of  $\text{H}_2$ . Then, the catalysts were exposed to  $\text{O}_2$  (after purging with He),  $\text{CO}_2$ ,  $\text{H}_2/\text{CO}_2$  ( $3:1$ ) or  $\text{H}_2$  in a gas flow of  $30 \text{ ml min}^{-1}$  at a pressure of  $1 \text{ bar}$ . For the high-pressure experiments, background spectra were recorded at  $180^\circ\text{C}$  under vacuum. Then, the catalysts were exposed to  $\text{CO}_2$ ,  $\text{H}_2$  or  $\text{H}_2/\text{CO}_2$  ( $3:1$ ) in a gas flow of  $30 \text{ ml min}^{-1}$  at a pressure of  $30 \text{ bar}$ . Spectra were recorded during the whole of the in situ DRIFT experiment.

Brunauer-Emmett-Teller surface area measurements were performed on a Micromeritics Tristar 3020 Surface Area Analyzer. Prior to  $\text{N}_2$  adsorption, the samples were degassed under vacuum at  $120^\circ\text{C}$  for  $6 \text{ h}$ .

**Computational details.** DFT calculations were performed using the Vienna Ab initio Simulation Package (VASP)<sup>56-59</sup>. The projector augmented-wave pseudopotential method with the Perdew-Burke-Ernzerhof (PBE) exchange-correlation functional and a plane-wave cut-off energy of  $400 \text{ eV}$  was adopted<sup>60-63</sup>. Grimme's zero-damping DFT-D3 method was used to calculate the van der Waals correction<sup>64,65</sup>. A trilayer model of  $\text{MoS}_2$  was built in a  $6 \times 6$  supercell (Extended Data Fig. 7b), and a nanoribbon model of  $\text{MoS}_2$  with six repeating units along the ribbon direction was built to simulate the edges, with the Mo edge saturated with S monomers and the S edge saturated with a combination of S monomers and dimers (Extended Data Fig. 7a)<sup>39,40</sup>. The vacuum thicknesses were set larger than  $15 \text{ \AA}$ . A Monkhorst-Pack  $k$ -point sampling of  $1 \times 1 \times 1$  was selected<sup>66</sup>. The fixed-bond-length method, as implemented in the Atomic Simulation Environment, was used to search for transition states<sup>67</sup>. In structural optimizations, the residual forces between atoms were converged to below  $0.02 \text{ eV \AA}^{-1}$ . The free energies of the reaction intermediates and transition states on the surface were calculated as  $E_{\text{total}} + \text{ZPE} + H_{\text{vib}} - TS_{\text{vib}}$ , where  $E_{\text{total}}$  is the DFT-calculated total energy, ZPE is the zero-point energy,  $T$  is the temperature and  $H_{\text{vib}}$  and  $S_{\text{vib}}$  are the enthalpy and entropy parts of non-imaginary vibrations derived from the harmonic approximation to the potential at the temperature  $T$ . The free energies of gas-phase molecules were calculated as  $E_{\text{total}} + \text{ZPE} + H - TS + RT \ln(P/P_0)$ , where  $H$  is the enthalpy and  $S$  is the entropy at the temperature  $T$  obtained using the ideal gas approximation,  $R$  is the gas

constant, which is  $8.314 \text{ J mol}^{-1} \text{ K}^{-1}$ ,  $P$  is the partial pressure of the gas-phase component, which is 1.25 MPa for  $\text{CO}_2$  and 3.75 MPa for  $\text{H}_2$ , and  $P_0$  is the standard pressure. A free-energy correction of 0.44 eV was added for the gas-phase  $\text{CO}_2$  molecule as described in ref.<sup>68</sup>.

The formation energies of  $\text{MoS}_2$  edges and S vacancies were calculated using the energies of  $\text{H}_2$ ,  $\text{H}_2\text{S}$  and intact  $\text{MoS}_2$  as references. S-edge S vacancies generated by removing one S from terminal S dimers are not active toward the adsorption of  $\text{CO}_2$  and  $\text{H}_2$  molecules, and removal of a terminal S monomer costs significantly more energy than removal from the Mo edge (Extended Data Fig. 7d). Thus, the S-edge vacancies were not considered in the calculation of the reaction mechanism. Brim S vacancies are less stable and can be facilely transformed into edge S vacancies with an energy gain of around 0.9 eV per Sv, and thus they were not considered further (Extended Data Fig. 7f). The dissociative adsorption energy ( $E_d$ ) of  $\text{H}_2$  on the in-plane S atoms is around 3.1 eV, indicating that in-plane S-H species can barely be formed. The dissociative adsorption of  $\text{H}_2$  on the S sites of the Mo edge is relatively easy, with a dissociative  $E_d$  of 0.34 eV (Extended Data Fig. 7e). However, they are both less favourable than the adsorption of  $\text{H}_2$  on the Mo sites of the Mo-edge S vacancies, with a dissociative  $E_d$  of, for example, -0.25 eV on the double-Sv. In addition, the reductive abilities of the Mo-H and S-H species were also compared by using the  $\text{CO}^*$  hydrogenation step as a probe reaction. The hydrogenation of  $\text{CO}^*$  by the S-H species needs to overcome a higher barrier of 1.34 eV compared with the hydrogenation by the Mo-H species, with a barrier of 0.34 eV on the double-Sv and 1.24 eV on the triple-Sv sites. Thus, these results show that the Mo-H species is more easily formed and is more reductive than the S-H species at the Mo edge, and therefore we only considered the Mo-H species as the reductant in the study of the reaction mechanism.

The reaction microkinetics were simulated using the CatMAP software<sup>63</sup>. The steady-state approximation was adopted for solving the reaction rate equations. The microkinetic reaction models used in this study are listed in Supplementary Table 3. The compensation effect was considered to obtain the prefactors for the rate-determining steps based on the experimental reaction kinetics<sup>69–71</sup>.

The chemical shifts of TMP adsorbed at the S vacancies were calculated with VASP using the linear response method<sup>72,73</sup>. A high cut-off energy of 600 eV and a convergence criterion of  $10^{-8}$  were adopted for the electronic iteration steps. The chemical shift of  $\text{H}_3\text{PO}_4$  as reference was obtained by using the calculated chemical shift of the  $(\text{NH}_4)_2\text{HPO}_4$  crystal structure minus 1.13 ppm, which is the experimental chemical shift of  $\text{H}_3\text{PO}_4$  relative to that of  $(\text{NH}_4)_2\text{HPO}_4$ . The supercell of the  $(\text{NH}_4)_2\text{HPO}_4$  crystal structure was obtained from the Crystallography Open Database. Chemical shifts were calculated after fully optimizing the adsorption structures, as shown in Extended Data Fig. 6a. Three and four TMP molecules can be stably adsorbed on the double-Sv and triple-Sv sites at the Mo edge, respectively, whereas only one TMP can be stably adsorbed on the in-plane double-Sv and triple-Sv sites owing to steric hindrance effects.

## Data availability

The data supporting the findings of this study are available within the article and its Supplementary Information or from the corresponding authors upon reasonable request. The atomic positions of the reaction intermediates are available in the figshare repository (<https://doi.org/10.6084/m9.figshare.13498254.v1>).

Received: 9 July 2020; Accepted: 25 January 2021;

Published online: 22 March 2021

## References

- Aresta, M., Dibenedetto, A. & Angelini, A. Catalysis for the valorization of exhaust carbon: from  $\text{CO}_2$  to chemicals, materials, and fuels. Technological use of  $\text{CO}_2$ . *Chem. Rev.* **114**, 1709–1742 (2014).
- Song, C. S. Global challenges and strategies for control, conversion and utilization of  $\text{CO}_2$  for sustainable development involving energy, catalysis, adsorption and chemical processing. *Catal. Today* **115**, 2–32 (2006).
- Goepfert, A. et al. Recycling of carbon dioxide to methanol and derived products – closing the loop. *Chem. Soc. Rev.* **43**, 7995–8048 (2014).
- Appel, A. M. et al. Frontiers, opportunities, and challenges in biochemical and chemical catalysis of  $\text{CO}_2$  fixation. *Chem. Rev.* **113**, 6621–6658 (2013).
- Wang, W., Wang, S., Ma, X. & Gong, J. Recent advances in catalytic hydrogenation of carbon dioxide. *Chem. Soc. Rev.* **40**, 3703–3727 (2011).
- Kondratenko, E. V. et al. Status and perspectives of  $\text{CO}_2$  conversion into fuels and chemicals by catalytic, photocatalytic and electrocatalytic processes. *Energy Environ. Sci.* **6**, 3112–3135 (2013).
- Yarulina, I. et al. Recent trends and fundamental insights in the methanol-to-hydrocarbons process. *Nat. Catal.* **1**, 398–411 (2018).
- Graciani, J. et al. Highly active copper-ceria and copper-ceria-titania catalysts for methanol synthesis from  $\text{CO}_2$ . *Science* **345**, 546–550 (2014).
- Tackett, B. M., Gomez, E. & Chen, J. G. Net reduction of  $\text{CO}_2$  via its thermocatalytic and electrocatalytic transformation reactions in standard and hybrid processes. *Nat. Catal.* **2**, 381–386 (2019).
- Wang, J. et al. A highly selective and stable  $\text{ZnO-ZrO}_2$  solid solution catalyst for  $\text{CO}_2$  hydrogenation to methanol. *Sci. Adv.* **3**, e1701290 (2017).
- Martin, O. et al. Indium oxide as a superior catalyst for methanol synthesis by  $\text{CO}_2$  hydrogenation. *Angew. Chem. Int. Ed.* **55**, 6261–6265 (2016).
- Frei, M. S. et al. Mechanism and microkinetics of methanol synthesis via  $\text{CO}_2$  hydrogenation on indium oxide. *J. Catal.* **361**, 313–321 (2018).
- Liu, X. et al. Selective transformation of carbon dioxide into lower olefins with a bifunctional catalyst composed of  $\text{ZnGa}_2\text{O}_4$  and SAPO-34. *Chem. Commun.* **54**, 140–143 (2018).
- Ni, Y. et al. Selective conversion of  $\text{CO}_2$  and  $\text{H}_2$  into aromatics. *Nat. Commun.* **9**, 3457 (2018).
- Gao, P. et al. Direct conversion of  $\text{CO}_2$  into liquid fuels with high selectivity over a bifunctional catalyst. *Nat. Chem.* **9**, 1019–1024 (2017).
- Gao, P. et al. Direct production of lower olefins from  $\text{CO}_2$  conversion via bifunctional catalysis. *ACS Catal.* **8**, 571–578 (2018).
- Jung, K. D. & Bell, A. T. Role of hydrogen spillover in methanol synthesis over  $\text{Cu/ZrO}_2$ . *J. Catal.* **193**, 207–223 (2000).
- Collins, S., Baltanas, M. & Bonivardi, A. An infrared study of the intermediates of methanol synthesis from carbon dioxide over  $\text{Pd}/\beta\text{-GaO}$ . *J. Catal.* **226**, 410–421 (2004).
- Conner, W. C. Jr & Falconer, J. L. Spillover in heterogeneous catalysis. *Chem. Rev.* **95**, 759–788 (1995).
- Rui, N. et al.  $\text{CO}_2$  hydrogenation to methanol over  $\text{Pd}/\text{In}_2\text{O}_3$ : effects of Pd and oxygen vacancy. *Appl. Catal. B* **218**, 488–497 (2017).
- Yin, Y. Z. et al.  $\text{Pd}@$ zeolitic imidazolate framework-8 derived  $\text{PdZn}$  alloy catalysts for efficient hydrogenation of  $\text{CO}_2$  to methanol. *Appl. Catal. B* **234**, 143–152 (2018).
- Kattel, S., Liu, P. & Chen, J. G. Tuning selectivity of  $\text{CO}_2$  hydrogenation reactions at the metal/oxide interface. *J. Am. Chem. Soc.* **139**, 9739–9754 (2017).
- Fisher, I. A. & Bell, A. T. In-situ infrared study of methanol synthesis from  $\text{H}_2/\text{CO}_2$  over  $\text{Cu}/\text{SiO}_2$  and  $\text{Cu}/\text{ZrO}_2/\text{SiO}_2$ . *J. Catal.* **172**, 222–237 (1997).
- Studt, F. et al. Discovery of a Ni-Ga catalyst for carbon dioxide reduction to methanol. *Nat. Chem.* **6**, 320–324 (2014).
- Behrens, M. et al. The active site of methanol synthesis over  $\text{Cu}/\text{ZnO}/\text{Al}_2\text{O}_3$  industrial catalysts. *Science* **336**, 893–897 (2012).
- Kuld, S. et al. Quantifying the promotion of Cu catalysts by ZnO for methanol synthesis. *Science* **352**, 969–974 (2016).
- Behrens, M. Heterogeneous catalysis of  $\text{CO}_2$  conversion to methanol on copper surfaces. *Angew. Chem. Int. Ed.* **53**, 12022–12024 (2014).
- Zabitskiy, M. et al. The unique interplay between copper and zinc during catalytic carbon dioxide hydrogenation to methanol. *Nat. Commun.* **11**, 2409 (2020).
- Sehested, J. Industrial and scientific directions of methanol catalyst development. *J. Catal.* **371**, 368–375 (2019).
- Behrens, M. Promoting the synthesis of methanol: understanding the requirements for an industrial catalyst for the conversion of  $\text{CO}_2$ . *Angew. Chem. Int. Ed.* **55**, 14906–14908 (2016).
- Schlögl, R. Heterogeneous catalysis. *Angew. Chem. Int. Ed.* **54**, 3465–3520 (2015).
- Liu, G. et al.  $\text{MoS}_2$  monolayer catalyst doped with isolated Co atoms for the hydrodeoxygenation reaction. *Nat. Chem.* **9**, 810–816 (2017).
- Cai, L. et al. Vacancy-induced ferromagnetism of  $\text{MoS}_2$  nanosheets. *J. Am. Chem. Soc.* **137**, 2622–2627 (2015).
- Chianelli, R. R., Daage, M. & Ledoux, M. J. Fundamental studies of transition-metal sulfide catalytic materials. *Adv. Catal.* **40**, 177–232 (1994).
- Okamoto, Y. et al. Structure of the active sites of Co–Mo hydrodesulfurization catalysts as studied by magnetic susceptibility measurement and NO adsorption. *J. Phys. Chem. B* **109**, 288–296 (2005).
- Weber, T. et al. Basic reaction steps in the sulfidation of crystalline  $\text{MoO}_3$  to  $\text{MoS}_2$  as studied by X-ray photoelectron and infrared emission spectroscopy. *J. Phys. Chem.* **100**, 14144–14150 (1996).
- Peng, Y.-K. et al. Trimethylphosphine-assisted surface fingerprinting of metal oxide nanoparticle by  $^{31}\text{P}$  solid-state NMR: a zinc oxide case study. *J. Am. Chem. Soc.* **138**, 2225–2234 (2016).
- Zhou, J. et al. A library of atomically thin metal chalcogenides. *Nature* **556**, 355–359 (2018).
- Raybaud, P. et al. Ab initio study of the  $\text{H}_2\text{-H}_2\text{S}/\text{MoS}_2$  gas–solid interface: the nature of the catalytically active sites. *J. Catal.* **189**, 129–146 (2000).
- Tsai, C., Abild-Pedersen, F. & Norskov, J. K. Tuning the  $\text{MoS}_2$  edge-site activity for hydrogen evolution via support interactions. *Nano Lett.* **14**, 1381–1387 (2014).
- Larmier, K. et al.  $\text{CO}_2$ -to-methanol hydrogenation on zirconia-supported copper nanoparticles: reaction intermediates and the role of the metal-support interface. *Angew. Chem. Int. Ed.* **56**, 2318–2323 (2017).
- Kunke, E. L. et al. Hydrogenation of  $\text{CO}_2$  to methanol and CO on  $\text{Cu}/\text{ZnO}/\text{Al}_2\text{O}_3$ : is there a common intermediate or not? *J. Catal.* **328**, 43–48 (2015).
- Medford, A. J. et al. CatMAP: a software package for descriptor-based microkinetic mapping of catalytic trends. *Catal. Lett.* **145**, 794–807 (2015).
- Jaramillo, T. F. et al. Identification of active edge sites for electrochemical  $\text{H}_2$  evolution from  $\text{MoS}_2$  nanocatalysts. *Science* **317**, 100–102 (2007).

45. Hinnemann, B. et al. Biomimetic hydrogen evolution: MoS<sub>2</sub> nanoparticles as catalyst for hydrogen evolution. *J. Am. Chem. Soc.* **127**, 5308–5309 (2005).
46. Byskov, L. S., Nørskov, J. K., Clausen, B. S. & Topsøe, H. DFT calculations of unpromoted and promoted MoS<sub>2</sub>-based hydrodesulfurization catalysts. *J. Catal.* **187**, 109–122 (1999).
47. Prins, R., De Beer, V. H. J. & Somorjai, G. A. Structure and function of the catalyst and the promoter in Co–Mo hydrodesulfurization catalysts. *Catal. Rev.* **31**, 1–41 (1989).
48. Duyar, M. S. et al. A highly active molybdenum phosphide catalyst for methanol synthesis from CO and CO<sub>2</sub>. *Angew. Chem. Int. Ed.* **57**, 15045–15050 (2018).
49. Posada-Pérez, S. et al. The bending machine: CO<sub>2</sub> activation and hydrogenation on δ-MoC(001) and β-Mo<sub>2</sub>C(001) surfaces. *Phys. Chem. Chem. Phys.* **16**, 14912–14921 (2014).
50. Deng, J. et al. Triggering the electrocatalytic hydrogen evolution activity of the inert two-dimensional MoS<sub>2</sub> surface via single-atom metal doping. *Energy Environ. Sci.* **8**, 1594–1601 (2015).
51. Wang, S., Goulas, K. & Iglesia, E. Condensation and esterification reactions of alkanals, alkanones, and alkanols on TiO<sub>2</sub>: elementary steps, site requirements, and synergistic effects of bifunctional strategies. *J. Catal.* **340**, 302–320 (2016).
52. Chinchin, G., Hay, C., Vandervell, H. & Waugh, K. The measurement of copper surface areas by reactive frontal chromatography. *J. Catal.* **103**, 79–86 (1987).
53. Luo, L. et al. Gas-phase reaction network of Li/MgO-catalyzed oxidative coupling of methane and oxidative dehydrogenation of ethane. *ACS Catal.* **9**, 2514–2520 (2019).
54. Zhou, Z. et al. The vacuum ultraviolet beamline/endstations at NSRL dedicated to combustion research. *J. Synchrotron Radiat.* **23**, 1035–1045 (2016).
55. Li, Y. Y. et al. Disclosure of the surface composition of TiO<sub>2</sub>-supported gold palladium bimetallic catalysts by high-sensitivity low-energy ion scattering spectroscopy. *ACS Catal.* **8**, 1790–1795 (2018).
56. Kresse, G. & Hafner, J. Ab initio molecular dynamics for liquid metals. *Phys. Rev. B* **47**, 558–561 (1993).
57. Kresse, G. & Hafner, J. Ab initio molecular-dynamics simulation of the liquid-metal-amorphous-semiconductor transition in germanium. *Phys. Rev. B* **49**, 14251–14269 (1994).
58. Kresse, G. & Furthmüller, J. Efficiency of ab-initio total energy calculations for metals and semiconductors using a plane-wave basis set. *Comput. Mater. Sci.* **6**, 15–50 (1996).
59. Kresse, G. & Furthmüller, J. Efficient iterative schemes for ab initio total-energy calculations using a plane-wave basis set. *Phys. Rev. B* **54**, 11169–11186 (1996).
60. Blochl, P. E. Projector augmented-wave method. *Phys. Rev. B* **50**, 17953–17979 (1994).
61. Kresse, G. & Joubert, D. From ultrasoft pseudopotentials to the projector augmented-wave method. *Phys. Rev. B* **59**, 1758–1775 (1999).
62. Perdew, J. P., Burke, K. & Ernzerhof, M. Generalized gradient approximation made simple. *Phys. Rev. Lett.* **77**, 3865–3868 (1996).
63. Perdew, J. P., Burke, K. & Ernzerhof, M. Generalized gradient approximation made simple. *Phys. Rev. Lett.* **77**, 3865 (1996); erratum **78**, 1396 (1997).
64. Grimme, S., Antony, J., Ehrlich, S. & Krieg, H. A consistent and accurate ab initio parametrization of density functional dispersion correction (DFT-D) for the 94 elements H–Pu. *J. Chem. Phys.* **132**, 154104 (2010).
65. Grimme, S., Ehrlich, S. & Goerigk, L. Effect of the damping function in dispersion corrected density functional theory. *J. Comput. Chem.* **32**, 1456–1465 (2011).
66. Monkhorst, H. J. & Pack, J. D. Special points for Brillouin-zone integrations. *Phys. Rev. B* **13**, 5188–5192 (1976).
67. Larsen, A. H. et al. The atomic simulation environment—a Python library for working with atoms. *J. Phys. Condens. Matter* **29**, 273002 (2017).
68. Studt, F. et al. The mechanism of CO and CO<sub>2</sub> hydrogenation to methanol over Cu-based catalysts. *ChemCatChem* **7**, 1105–1111 (2015).
69. Peacock-López, E. & Suhl, H. Compensation effect in thermally activated processes. *Phys. Rev. B* **26**, 3774–3782 (1982).
70. McCoy, B. J. Compensation effect in the dissociation of anharmonic oscillators: a model for catalysis. *J. Chem. Phys.* **80**, 3629–3631 (1984).
71. Bond, G. C., Keane, M. A., Kral, H. & Lercher, J. A. Compensation phenomena in heterogeneous catalysis: general principles and a possible explanation. *Catal. Rev.* **42**, 323–383 (2000).
72. Pickard, C. J. & Mauri, F. All-electron magnetic response with pseudopotentials: NMR chemical shifts. *Phys. Rev. B* **63**, 245101 (2001).
73. Yates, J. R., Pickard, C. J. & Mauri, F. Calculation of NMR chemical shifts for extended systems using ultrasoft pseudopotentials. *Phys. Rev. B* **76**, 024401 (2007).
74. Thrane, J. et al. Methanol-assisted autocatalysis in catalytic methanol synthesis. *Angew. Chem. Int. Ed.* **59**, 18189–18193 (2020).
75. Gao, P. et al. Influence of Zr on the performance of Cu/Zn/Al/Zr catalysts via hydroxalcalite-like precursors for CO<sub>2</sub> hydrogenation to methanol. *J. Catal.* **298**, 51–60 (2013).
76. Tisseraud, C. et al. The Cu–ZnO synergy in methanol synthesis from CO<sub>2</sub>, part 2: origin of the methanol and CO selectivities explained by experimental studies and a sphere contact quantification model in randomly packed binary mixtures on Cu–ZnO coprecipitate catalysts. *J. Catal.* **330**, 533–544 (2015).
77. van den Berg, R. et al. Support functionalization to retard Ostwald ripening in copper methanol synthesis catalysts. *ACS Catal.* **5**, 4439–4448 (2015).
78. van den Berg, R. et al. Structure sensitivity of Cu and CuZn catalysts relevant to industrial methanol synthesis. *Nat. Commun.* **7**, 13057 (2016).
79. Boudart, M. Turnover rates in heterogeneous catalysis. *Chem. Rev.* **95**, 661–666 (1995).
80. Deng, J. et al. High-performance hydrogen evolution electrocatalysis by layer-controlled MoS<sub>2</sub> nanosheets. *RSC Adv.* **4**, 34733–34738 (2014).
81. Zeng, T. et al. Density functional theory study of CO adsorption on molybdenum sulfide. *J. Phys. Chem. B* **109**, 2846–2854 (2005).
82. Travert, A. et al. Parallel between infrared characterisation and ab initio calculations of CO adsorption on sulphided Mo catalysts. *Catal. Today* **70**, 255–269 (2001).
83. Uvdal, P., Weldon, M. K. & Friend, C. M. Adsorbate symmetry and Fermi resonances of methoxide adsorbed on Mo(110) as studied by surface infrared spectroscopy. *Phys. Rev. B* **50**, 12258–12261 (1994).
84. Guyon, P. M., Chupka, W. A. & Berkowitz, J. Photoionization mass spectrometric study of formaldehyde H<sub>2</sub>CO, HDCO and D<sub>2</sub>CO. *J. Chem. Phys.* **64**, 1419–1436 (1976).
85. Berkowitz, J. Photoionization of CH<sub>3</sub>OH, CD<sub>3</sub>OH, and CH<sub>3</sub>OD: dissociative ionization mechanisms and ionic structures. *J. Chem. Phys.* **69**, 3044–3054 (1978).

## Acknowledgements

We acknowledge the financial support from the Ministry of Science and Technology of China (Nos. 2016YFA0204100, 2016YFA0200200, 2017YFA0402800 and 2017YFB0602201), the National Natural Science Foundation of China (Nos. 21890753, 21988101, 91545203 and 21433008), the Key Research Program of Frontier Sciences of the Chinese Academy of Sciences (No. QYZDB-SSW-JSC020), the Strategic Priority Research Program of the Chinese Academy of Sciences (No. XDB36030200) and the DNL Cooperation Fund, CAS (No. DNL180201). We thank the staff at the BL14W1 beamline of the Shanghai Synchrotron Radiation Facilities for assistance with the EXAFS and XANES measurements. We also thank H. Su for assistance in the DFT calculations.

## Author contributions

D.D. and Ye W. conceived and designed the experiments. J.H. performed the materials synthesis, characterization and performance experiments. L.Y. contributed to the DFT calculations. J.D. assisted with the materials synthesis. Yong W., K.C., Q.Z. and R.H. assisted with data analysis and manuscript revision. C.M. conducted the HAADF-STEM experiments. S.Z. assisted with the HRTEM experiments. W.W., S.Y., Y.P., J.Y., H.M. and F.Q. conducted the SVUV-PIMS experiments. Yongke W., Y.Z. and M.-S.C. assisted with the XPS and HS-LEIS experiments. Z.Z., G.H. and X.H. conducted the NMR experiments and analysed the data. X.M. and R.H. assisted with the in situ EPR experiments. Q.J. assisted with the NO adsorption experiments. J.M. assisted with the O<sub>2</sub> adsorption experiments. X.B. provided constructive suggestions. J.H., L.Y., Ye W. and D.D. wrote the paper.

## Competing interests

The authors declare no competing interests.

## Additional information

**Extended data** is available for this paper at <https://doi.org/10.1038/s41929-021-00584-3>.

**Supplementary information** The online version contains supplementary material available at <https://doi.org/10.1038/s41929-021-00584-3>.

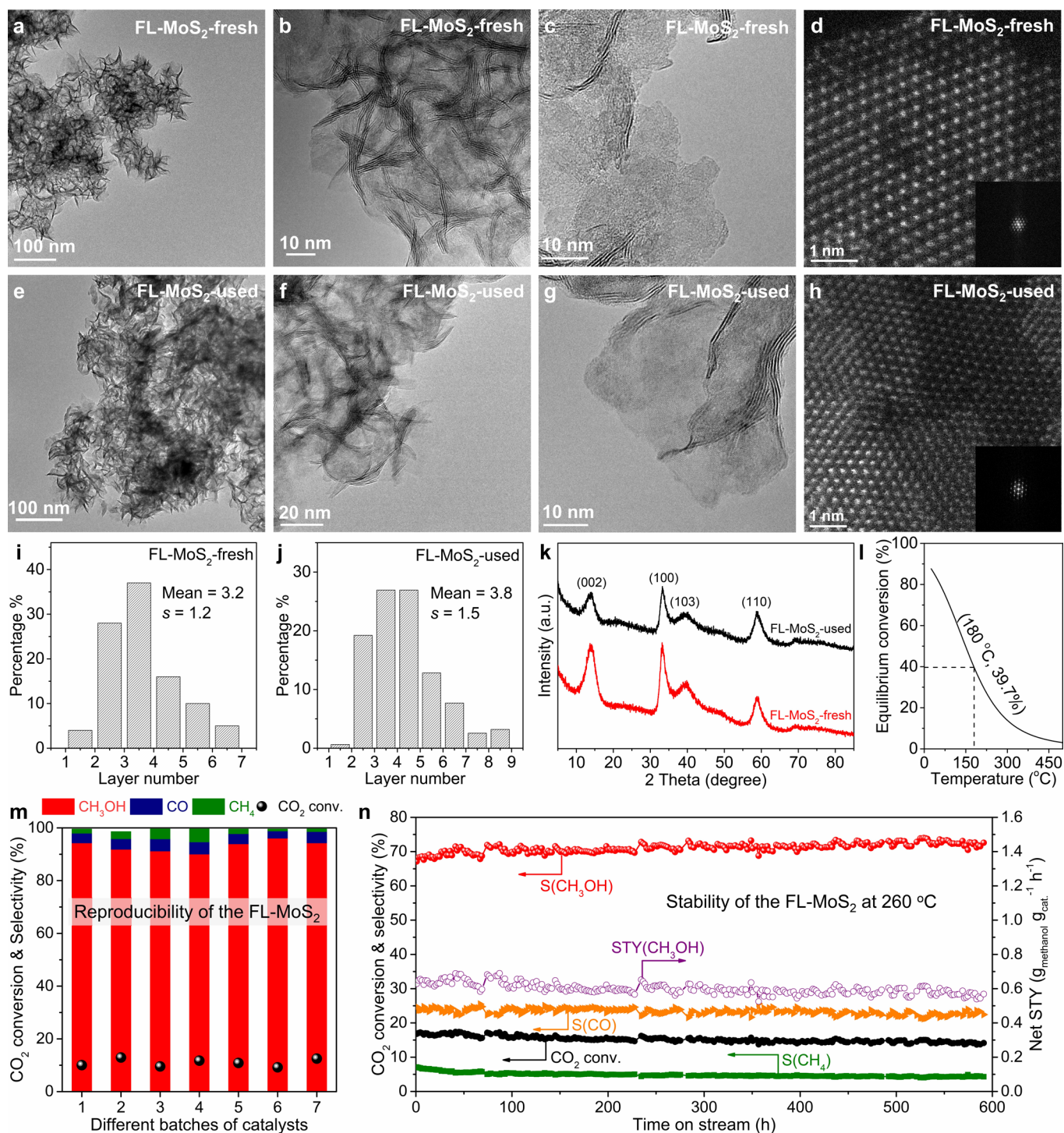
**Correspondence and requests for materials** should be addressed to Y.W. or D.D.

**Peer review information** *Nature Catalysis* thanks Jose Rodriguez and the other, anonymous, reviewer(s) for their contribution to the peer review of this work.

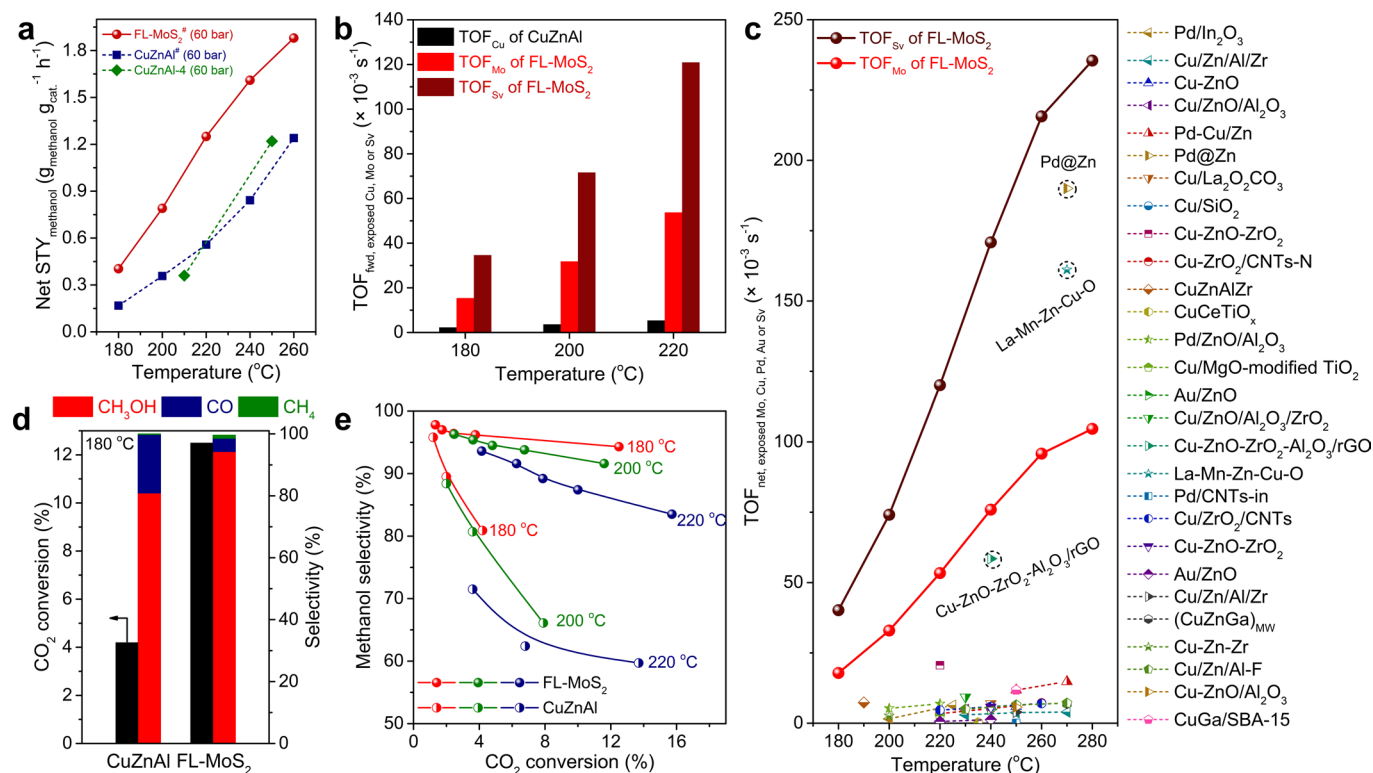
**Reprints and permissions information** is available at [www.nature.com/reprints](http://www.nature.com/reprints).

**Publisher's note** Springer Nature remains neutral with regard to jurisdictional claims in published maps and institutional affiliations.

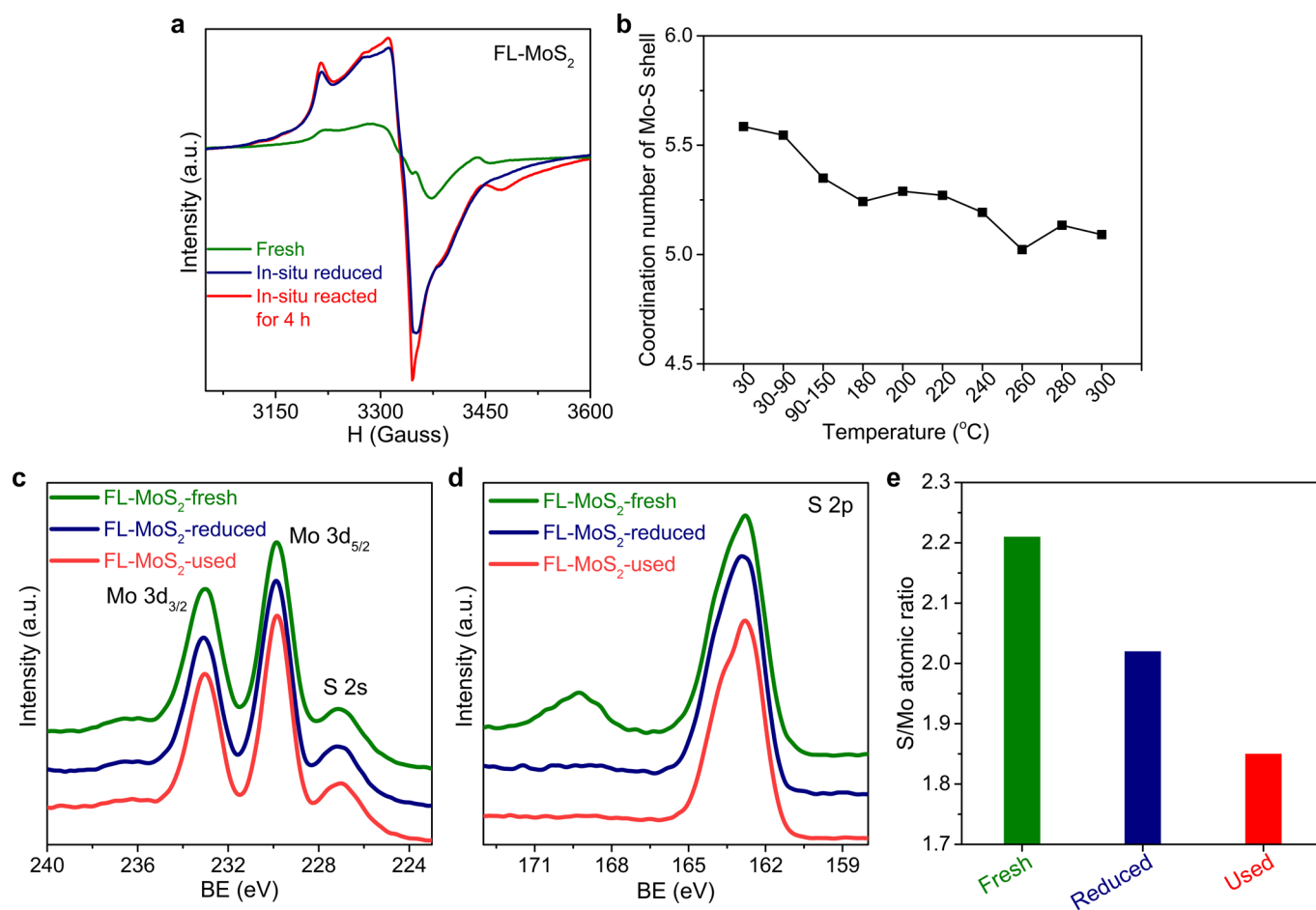
© The Author(s), under exclusive licence to Springer Nature Limited 2021



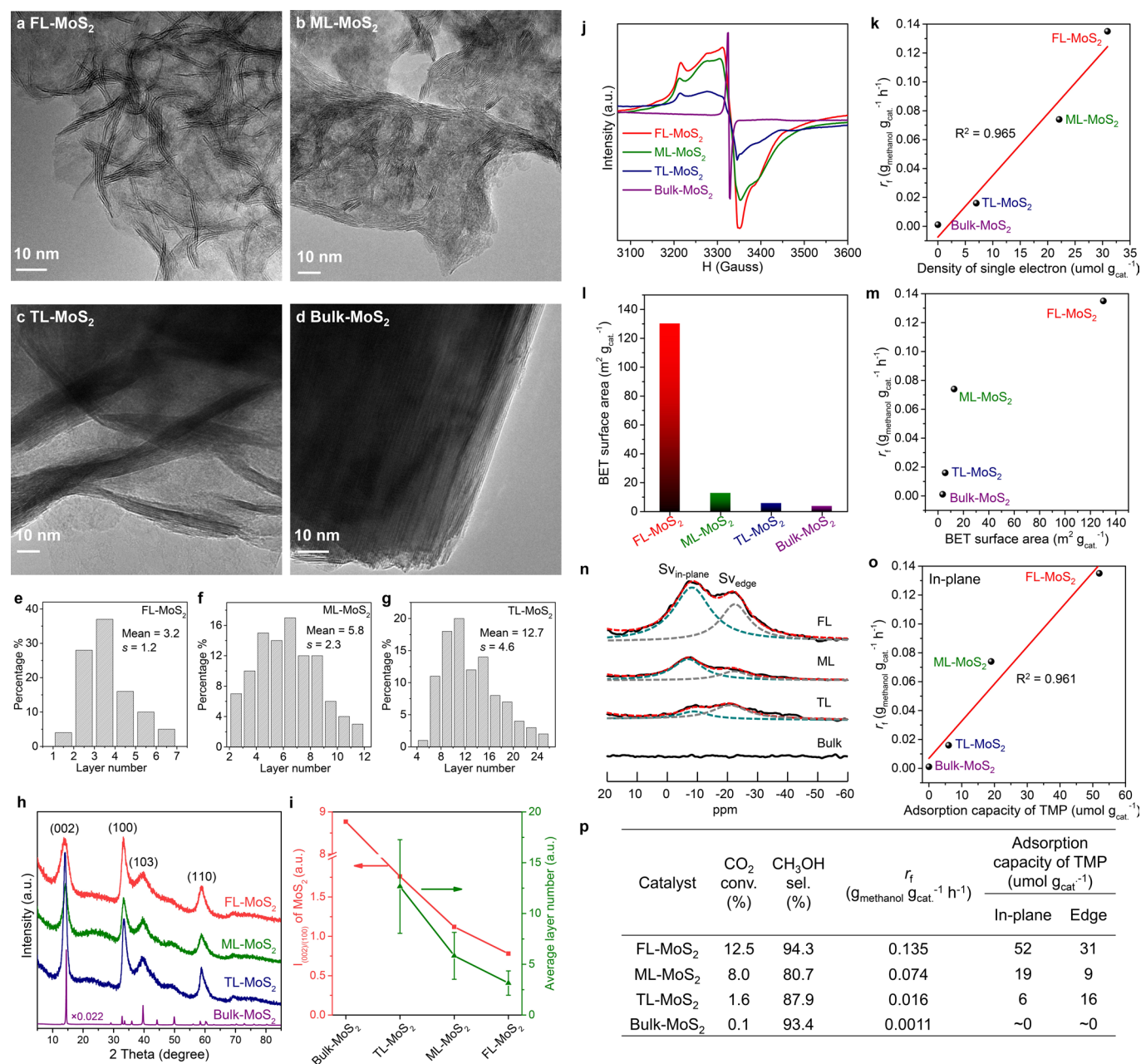
**Extended Data Fig. 1 | Structural stability, reproducibility and durability of the FL-MoS<sub>2</sub> catalyst.** **a-h**, TEM images of the fresh (**a-c**) and used FL-MoS<sub>2</sub> (after 3000 hours of durability test, **e-g**). HAADF-STEM images of the fresh FL-MoS<sub>2</sub> (**d**) and the used FL-MoS<sub>2</sub> (**h**) with the corresponding FFT patterns (inside). Both the fresh and the used FL-MoS<sub>2</sub> exhibit highly crystallized 2H-MoS<sub>2</sub> structures as reflected by the FFT patterns. **i,j**, Layer number statistics for at least 100 of MoS<sub>2</sub> layers of the fresh FL-MoS<sub>2</sub> (**i**) and the used FL-MoS<sub>2</sub> after 3000 hours of durability test (**j**) based on TEM results. **k**, XRD pattern of the fresh and used FL-MoS<sub>2</sub>. **l**, Equilibrium conversion of CO<sub>2</sub> as a function of temperature in the hydrogenation of CO<sub>2</sub> to methanol. Total pressure is 50 bar with H<sub>2</sub>/CO<sub>2</sub> ratio of 3. **m**, Reproducibility test of individually synthesized FL-MoS<sub>2</sub> catalysts. Catalysts were pretreated in-situ by H<sub>2</sub> at 300 °C for 3 hours. Reaction activity tests were performed at 3000 mL g<sub>cat</sub><sup>-1</sup> h<sup>-1</sup>, 180 °C, 50 bar and H<sub>2</sub>/CO<sub>2</sub> ratio of 3:1. **n**, Durability test of the FL-MoS<sub>2</sub> for CO<sub>2</sub> hydrogenation at 260 °C. Catalyst was pretreated in-situ by H<sub>2</sub> at 300 °C for 3 hours. Reaction activity test was performed at 15000 mL g<sub>cat</sub><sup>-1</sup> h<sup>-1</sup>, 260 °C, 50 bar and H<sub>2</sub>/CO<sub>2</sub> ratio of 3:1.



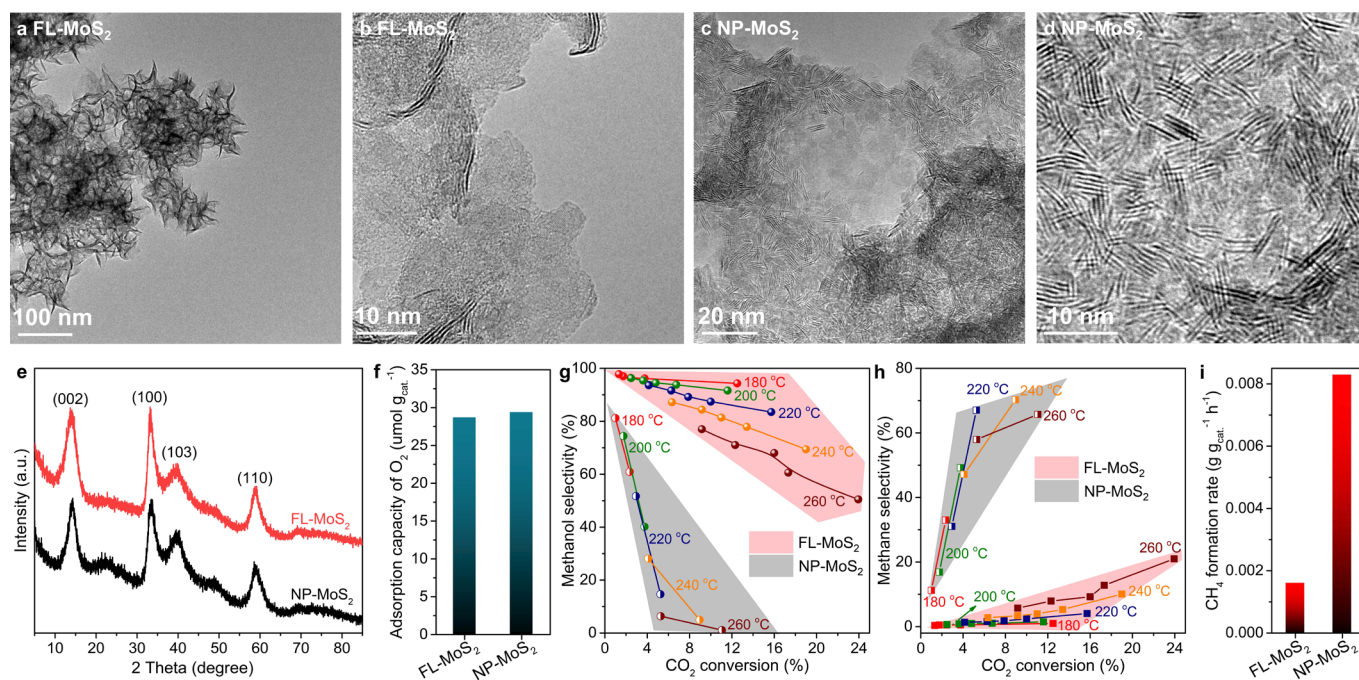
**Extended Data Fig. 2 | Comparison in catalytic performances of the FL-MoS<sub>2</sub> and the Cu/ZnO/Al<sub>2</sub>O<sub>3</sub> (CuZnAl) and other catalysts.** **a**, Comparison in net STY<sub>methanol</sub> over the Cu/ZnO/Al<sub>2</sub>O<sub>3</sub> (CuZnAl) and the FL-MoS<sub>2</sub> at 60 bar (Supplementary Table 1 for more details, # represents data of this work). **b**, Comparison in the forward TOF for methanol formation (calculated on the basis of the amount of exposed Cu, Mo or Sv sites) over the Cu/ZnO/Al<sub>2</sub>O<sub>3</sub> (CuZnAl) and the FL-MoS<sub>2</sub> at 50 bar and iso-conversion levels. It was reported that for the Cu/ZnO/Al<sub>2</sub>O<sub>3</sub> catalyst only small fractions of surface synergetic sites are considered to be highly active for the CO<sub>2</sub> conversion.<sup>25–30</sup> However, the real high-active sites can hardly be precisely quantified in the actual systems owing to the difficulty in identifying them based on the currently reported characterization techniques. Thus, in the calculation of the TOF, all surface Cu atoms are included in the amount of the active sites, as typically done in previous works<sup>74–78</sup>. The TOF on the Cu/ZnO/Al<sub>2</sub>O<sub>3</sub> catalyst calculated in this way should represent an average activity level of the active sites<sup>31,79</sup>. **c**, Comparison in the net TOF for methanol formation over the FL-MoS<sub>2</sub> and other state-of-the-art catalysts calculated on the basis of the amount of exposed metal (Supplementary Table 2 for more details, the order of catalysts in **(c)** corresponding to that in Supplementary Table 2). Reaction activity tests of the FL-MoS<sub>2</sub> were performed at 50 bar with a GHSV of 36000 mL g<sub>cat</sub><sup>-1</sup> h<sup>-1</sup>. **d**, The catalytic performances of the Cu/ZnO/Al<sub>2</sub>O<sub>3</sub> (CuZnAl) and the FL-MoS<sub>2</sub> under identical reaction conditions, which were tested at 180 °C, 50 bar and 3000 mL g<sub>cat</sub><sup>-1</sup> h<sup>-1</sup>. **e**, Selectivity to methanol as a function of CO<sub>2</sub> conversion over the FL-MoS<sub>2</sub> and the Cu/ZnO/Al<sub>2</sub>O<sub>3</sub> (CuZnAl) obtained by varying the GHSV in the range of 3000 to 36000 mL g<sub>cat</sub><sup>-1</sup> h<sup>-1</sup> at 50 bar and different temperatures. Catalysts were pretreated in-situ by H<sub>2</sub> at 300 °C for 3 hours. Reaction activity tests were performed using a tubular fixed-bed reactor with a H<sub>2</sub>/CO<sub>2</sub> ratio of 3. TOFs of the FL-MoS<sub>2</sub> were calculated on the basis of NO adsorption capacities.



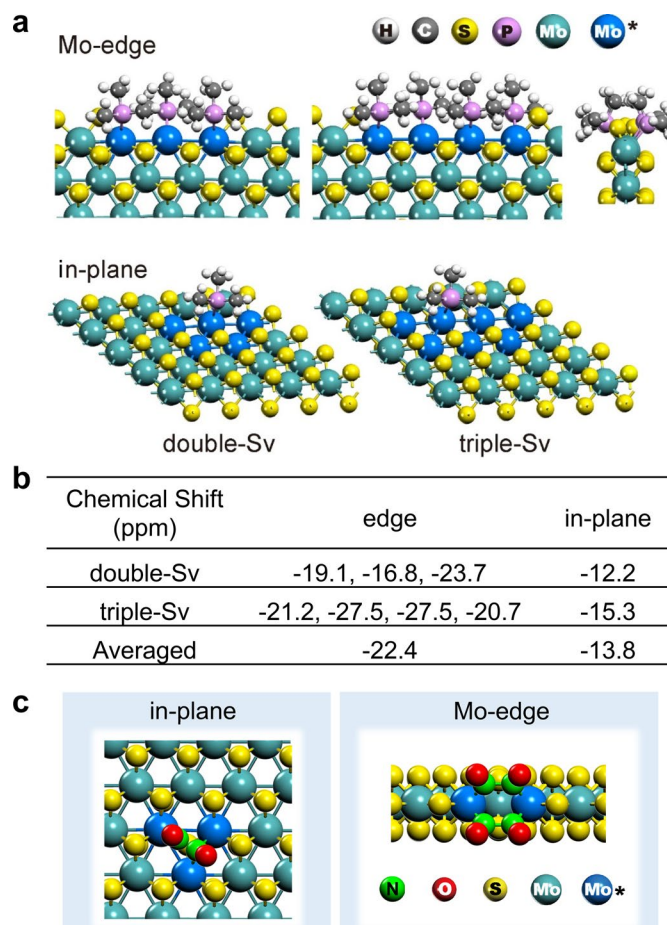
**Extended Data Fig. 3 | Characterizations of the FL-MoS<sub>2</sub> at different reaction stages.** **a**, In-situ EPR spectra of the fresh, in-situ reduced FL-MoS<sub>2</sub> and the FL-MoS<sub>2</sub> after in-situ reaction for 4 hours, respectively. Before measurements, the FL-MoS<sub>2</sub> was treated in-situ by H<sub>2</sub> (denoted as FL-MoS<sub>2</sub>-reduced), reaction gas (H<sub>2</sub>/CO<sub>2</sub> = 3/1, denoted as FL-MoS<sub>2</sub>-used) and purged with He without exposure to the air (see Methods for more details). **b**, Variation of the Mo-S coordination numbers of the FL-MoS<sub>2</sub> depending on the temperature during the H<sub>2</sub> pretreatment process. Debye-Waller factor ( $\sigma^2$ ) = 0.0041 ± 0.0002 Å<sup>2</sup>, inner potential correction ( $\Delta E_0$ ) = 2.7 ± 0.2 eV. Results show that the Mo-S coordination number decreases as the reduction temperature increases, which may be caused by the loss of sulphur atoms during H<sub>2</sub> treatment. **c, d**, XPS spectra of the fresh, reduced and used FL-MoS<sub>2</sub>, respectively. **e**, S/Mo atomic ratios in the fresh, reduced and used FL-MoS<sub>2</sub>, which were calculated based on the sensitivity factor and the peak area of the Mo 3d and S 2p, showing a decreasing trend.



**Extended Data Fig. 4 | Structure-activity relationship of different MoS<sub>2</sub> catalysts.** **a-d**, HRTEM images of the FL-MoS<sub>2</sub> (**a**), ML-MoS<sub>2</sub> (**b**), TL-MoS<sub>2</sub> (**c**) and Bulk-MoS<sub>2</sub> (**d**), respectively. **e-g**, Layer number statistics for at least 100 of MoS<sub>2</sub> layers of the FL-MoS<sub>2</sub> (**e**), ML-MoS<sub>2</sub> (**f**) and TL-MoS<sub>2</sub> (**g**), respectively, based on the HRTEM images. **h**, XRD patterns of different MoS<sub>2</sub> catalysts. These MoS<sub>2</sub> catalysts exhibit a typical hexagonal 2H-MoS<sub>2</sub> crystal, corresponding to PDF #37-1492. **i**, Correlations between the intensity ratio of the XRD (002) and (100) peaks ( $I_{(002)/(100)}$ ) and the layer thicknesses of different MoS<sub>2</sub> catalysts. Error bars represent the standard deviation for statistical layer numbers of different MoS<sub>2</sub> catalysts, respectively. The  $I_{(002)/(100)}$  of MoS<sub>2</sub> had been reported to assess the variation of layer numbers in a series of MoS<sub>2</sub> materials<sup>80</sup>. The increasing trend of  $I_{(002)/(100)}$  values of the FL-MoS<sub>2</sub> (0.78), ML-MoS<sub>2</sub> (1.12), TL-MoS<sub>2</sub> (1.76) and Bulk-MoS<sub>2</sub> (8.77) indicate the increasing layer numbers of these MoS<sub>2</sub> catalysts. **j**, In-situ EPR spectra of H<sub>2</sub>-pretreated MoS<sub>2</sub> samples (see Methods for more details). **k**, The correlation between the  $r_f$  for methanol formation and the density of single electron for the MoS<sub>2</sub> catalysts. 1,1-Diphenyl-2-picrylhydrazyl (DPPH) was used as an external standard to estimate the density of sulphur vacancies. **l**, BET surface area of different MoS<sub>2</sub> samples. **m**, The correlation between the  $r_f$  for methanol formation and the BET surface area of the MoS<sub>2</sub> catalysts. **n**, The <sup>31</sup>P MAS NMR spectra of in-situ H<sub>2</sub>-pretreated MoS<sub>2</sub> samples after full adsorption of TMP. The black lines are raw data and red lines are fitting results. **o**, The correlation between the  $r_f$  for methanol formation and the specific adsorption capacity of TMP for the MoS<sub>2</sub> catalysts. **p**, CO<sub>2</sub> hydrogenation performances and TMP adsorption capacities of different MoS<sub>2</sub> catalysts. Catalysts were pretreated in-situ by H<sub>2</sub> at 300 °C for 3 hours. Reaction activity tests were performed at 3000 mL g<sub>cat.</sub><sup>-1</sup> h<sup>-1</sup>, 180 °C, 50 bar and H<sub>2</sub>/CO<sub>2</sub> ratio of 3:1.



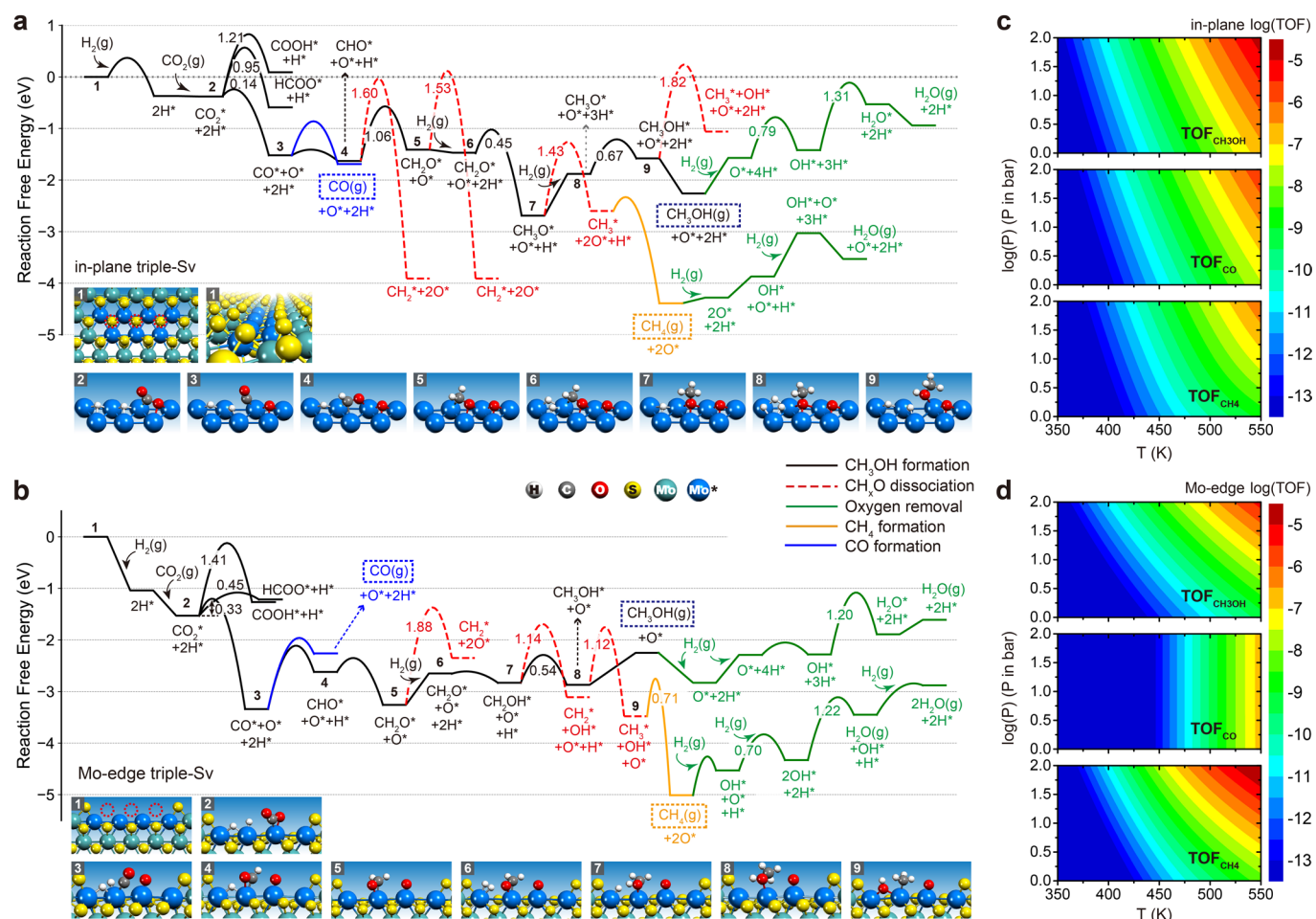
**Extended Data Fig. 5 | Characterizations of the structures and catalytic performances of the FL-MoS<sub>2</sub> and the NP-MoS<sub>2</sub>.** **a,b**, TEM images of the fresh FL-MoS<sub>2</sub>. **c,d**, TEM images of the fresh NP-MoS<sub>2</sub>. **e**, XRD patterns of the fresh FL-MoS<sub>2</sub> and NP-MoS<sub>2</sub>. These MoS<sub>2</sub> catalysts exhibit a typical hexagonal 2H-MoS<sub>2</sub> crystal, corresponding to PDF #37-1492. **f**, Adsorption capacity of O<sub>2</sub> over the reduced FL-MoS<sub>2</sub> and NP-MoS<sub>2</sub>. **g,h**, Selectivity of methanol and methane as a function of CO<sub>2</sub> conversion over the FL-MoS<sub>2</sub> and the NP-MoS<sub>2</sub> obtained by varying the GHSV at different temperatures. Catalysts were pretreated in-situ by H<sub>2</sub> at 300 °C for 3 hours. Reaction activity tests were performed using a tubular fixed-bed reactor at 50 bar and H<sub>2</sub>/CO<sub>2</sub> of 3. **i**, Formation rate of CH<sub>4</sub> from methanol decomposition over the FL-MoS<sub>2</sub> and NP-MoS<sub>2</sub> after H<sub>2</sub>-pretreatment. Liquid methanol (0.01 mL min<sup>-1</sup>) and high purity H<sub>2</sub> with 5% Ar with a gas flow rate of 30 mL min<sup>-1</sup> were simultaneously fed into the tubular fixed-bed reactor loaded with 200 mg catalyst at 1 bar and 180 °C.



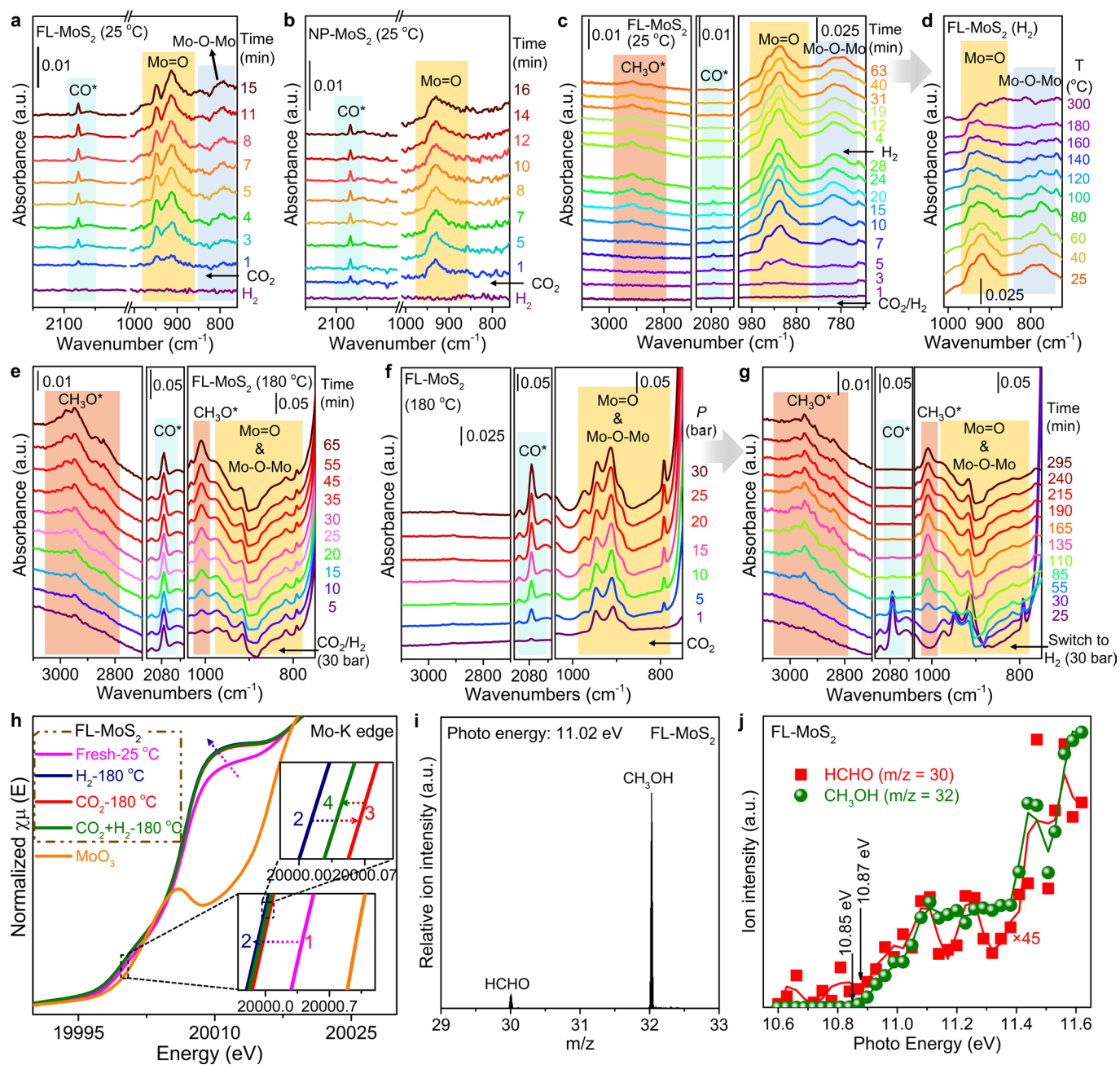
**Extended Data Fig. 6 | Optimized structures of adsorbed TMP and NO, and the chemical shifts of  $^{31}\text{P}$  of TMP molecules at the edge and basal plane.**

**a**, Optimized structures of adsorbed TMP at the edge and basal plane, respectively. The edge double-Sv and triple-Sv sites are fully covered by three and four TMP molecules, respectively, with differential adsorption free energies ( $G_{\text{ads}}$ ) of  $-0.39$  and  $-0.38$  eV at 100% coverage. The in-plane double-Sv and triple-Sv sites can adsorb only one TMP molecule with  $G_{\text{ads}}$  of  $-0.29$  and  $-0.18$  eV, respectively. **b**, DFT-calculated chemical shifts of  $^{31}\text{P}$  of TMP molecules adsorbed at the double-Sv and triple-Sv sites of  $\text{MoS}_2$  edges and basal plane. The chemical shift of  $\text{H}_3\text{PO}_4$  was used as the reference, and the calculated chemical shift of  $(\text{NH}_4)_2\text{HPO}_4$  was corrected by subtracting 1.13 ppm (the experimental chemical shift of  $(\text{NH}_4)_2\text{HPO}_4$  is 1.13 ppm relative to that of  $\text{H}_3\text{PO}_4$ ). **c**, DFT-calculated adsorption structures of NO at the in-plane and Mo-edge S vacancies.



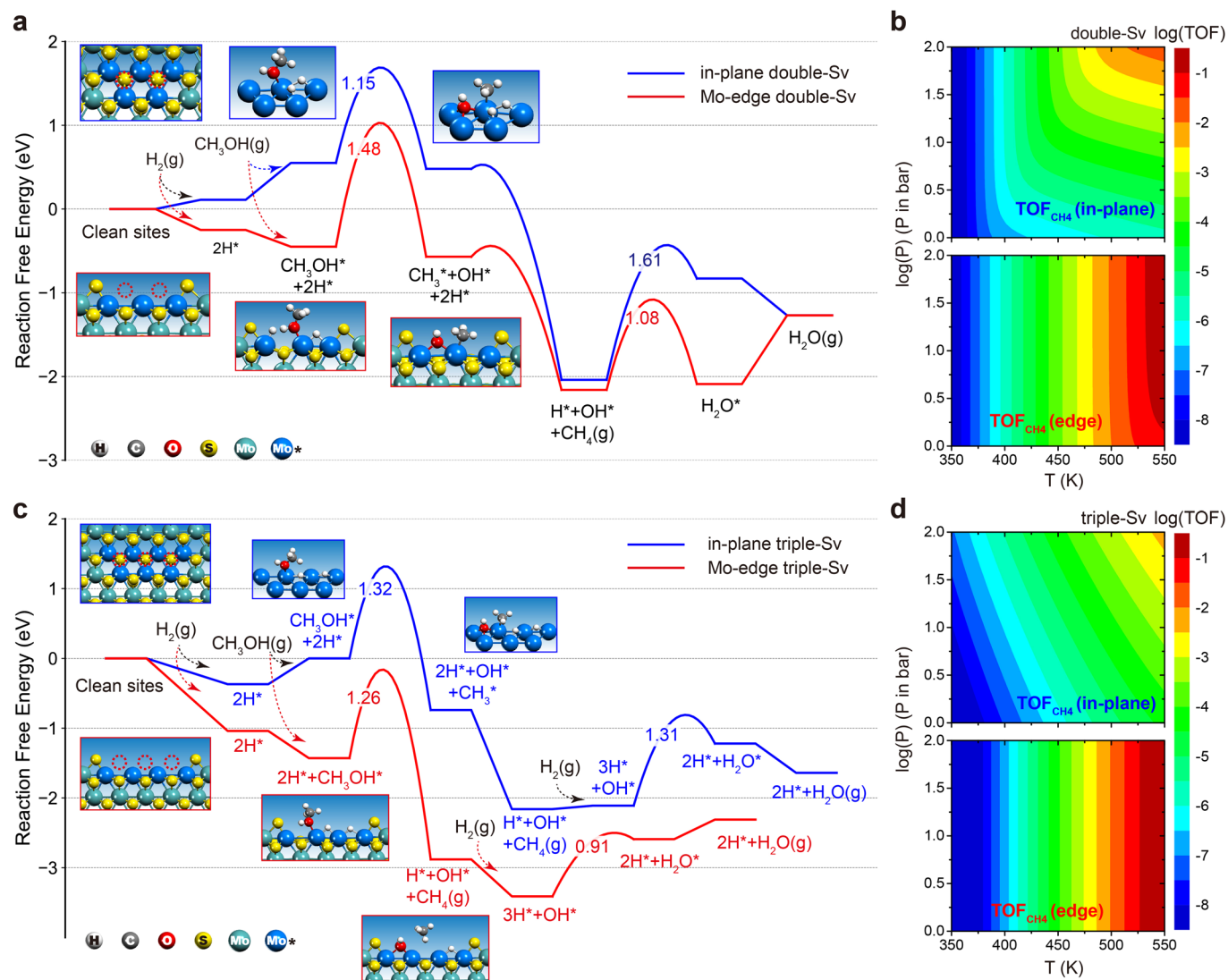


**Extended Data Fig. 8 | DFT studies of the reaction mechanisms of  $\text{CO}_2$  hydrogenation over the triple-Sv of  $\text{MoS}_2$ .** **a, b**, Free energy diagram of the  $\text{CO}_2$  hydrogenation reaction pathways on the in-plane and Mo-edge triple-Sv, respectively. Insets show the atomic structures of the S vacancies and the reaction intermediates. The red dotted circles in structures 1 denote the positions of S vacancies. **c, d**, Turnover frequencies (TOFs) for the generation of  $\text{CH}_3\text{OH}$ , CO and  $\text{CH}_4$  from the micro-kinetics modelling of the reaction mechanisms at the in-plane (**c**) and Mo-edge (**d**) triple-Sv, respectively.



Extended Data Fig. 9 | See next page for caption.

**Extended Data Fig. 9 | Identification of the CO<sub>2</sub> hydrogenation mechanism.** **a, b**, In-situ DRIFT spectra of CO<sub>2</sub> dissociation over the FL-MoS<sub>2</sub> (**a**) and the NP-MoS<sub>2</sub> (**b**) at 25 °C. As H<sub>2</sub> was switched to CO<sub>2</sub>, the linearly absorbed CO species (~2078 cm<sup>-1</sup>, **a, b**)<sup>81,82</sup>, the Mo=O species (peaks at 900 - 960 cm<sup>-1</sup>, **a, b**) and the Mo-O-Mo species (broad band at around 700 - 860 cm<sup>-1</sup>, **a**)<sup>36</sup> were observed, indicating that the coordinatively unsaturated Mo can easily dissociate CO<sub>2</sub> to \*CO and \*O at 25 °C. **c**, In-situ DRIFTS of the CO<sub>2</sub> hydrogenation and then H<sub>2</sub> reduction process at 25 °C. The reduced FL-MoS<sub>2</sub> catalyst was exposed to CO<sub>2</sub>/H<sub>2</sub> (1/3) reaction gas in a gas flow of 30 mL min<sup>-1</sup>. The formation of \*CO and O\* species<sup>36,81,82</sup> were observed. With the increase of reaction time, the peaks in the range from 2800-3000 cm<sup>-1</sup> grew up, which were attributed to the CH<sub>3</sub>O\* species<sup>83</sup>. When switching gas flow from the reaction gas to pure H<sub>2</sub>, the CO\* disappeared and the CH<sub>3</sub>O\* and O\* decreased gradually. **d**, In-situ DRIFTS of the H<sub>2</sub> reduction process with increasing temperatures. As the temperature increases from 25 to 300 °C, the O\* species can be gradually removed by the H<sub>2</sub>. **e**, In-situ DRIFT spectra of CO<sub>2</sub> hydrogenation over the FL-MoS<sub>2</sub> catalyst at 30 bar and 180 °C with a CO<sub>2</sub>/H<sub>2</sub> ratio of 1/3. **f**, In-situ DRIFT spectra of CO<sub>2</sub> dissociation over the FL-MoS<sub>2</sub> at 180 °C and 30 bar. **g**, In-situ DRIFT spectra of the FL-MoS<sub>2</sub> after switching the feed gas from CO<sub>2</sub> to H<sub>2</sub> at 180 °C and 30 bar. The line segments denote the scale bars of the absorbance. **h**, In-situ Mo K-edge XANES of the FL-MoS<sub>2</sub>. After the first spectrum of the fresh FL-MoS<sub>2</sub> catalyst was obtained, the catalyst was treated in-situ by H<sub>2</sub> at 300 °C for 3 hours. Then, the catalyst was cooled down to 180 °C under H<sub>2</sub> atmosphere, and the second spectrum was obtained. After that, the catalyst was exposed to CO<sub>2</sub> in a gas flow of 30 mL min<sup>-1</sup>, and the third spectrum was obtained. Subsequently, the feeding gas was switched to the reaction gas (H<sub>2</sub>/CO<sub>2</sub> = 3/1) with a gas flow of 30 mL min<sup>-1</sup>, and the fourth spectrum was obtained. **i**, In-situ SVUV-PIMS detection of gas-phase products during the CO<sub>2</sub> hydrogenation process. **j**, Photoionization efficiency spectra of the signals of m/z 30 and 32 during the CO<sub>2</sub> hydrogenation process. The FL-MoS<sub>2</sub> catalyst was pretreated in-situ by H<sub>2</sub> at 300 °C for 1 hour. After that, CO<sub>2</sub>/H<sub>2</sub> (1/3) was led through the reduced FL-MoS<sub>2</sub> catalyst at 180 °C and 5 bar. The signals of m/z 30 and 32 give ionization thresholds of 10.87 and 10.85 eV that agree well with the ionization thresholds of formaldehyde (HCHO) and methanol (CH<sub>3</sub>OH)<sup>84,85</sup>, respectively, demonstrating the existence of HCHO species during the CO<sub>2</sub> hydrogenation reaction.



**Extended Data Fig. 10 | DFT studies of the dissociation of methanol in  $H_2$  on the S vacancies of  $MoS_2$ .** **a, c**, The dissociation reaction mechanisms of methanol in  $H_2$  on the in-plane and Mo-edge double-Sv (**a**) and triple-Sv (**c**), respectively. Insets show the structures of the reaction intermediates. Dotted red circles denote the S vacancies. **b, d**, Turnover frequencies (TOFs) for the generation of methane from the micro-kinetics modelling of the reaction mechanisms at the double-Sv (**b**) and triple-Sv (**d**), respectively.